DUAL AND SINGLE COLOR MID-WAVELENGTH INFRARED QUANTUM WELL PHOTODETECTORS

A THESIS SUBMITTED TO
THE GRADUATE SCHOOL OF NATURAL AND APPLIED SCIENCES
OF
MIDDLE EAST TECHNICAL UNIVERSITY

BY

MELİH KALDIRIM

IN PARTIAL FULFILLMENT OF THE REQUIREMENTS
FOR
THE DEGREE OF MASTER OF SCIENCE
IN
ELECTRICAL AND ELECTRONICS ENGINEERING

SEPTEMBER 2008

Approval of the thesis:

DUAL AND SINGLE COLOR MID-WAVELENGTH INFRARED QUANTUM WELL PHOTODETECTORS

submitted by **MELİH KALDIRIM** in partial fulfillment of the requirements for the degree of **Master of Science in Electrical and Electronics Engineering Department, Middle East Technical University** by,

Prof. Dr. Canan Özgen _____
Dean, Graduate School of **Natural and Applied Sciences**

Prof. Dr. İsmet Erkmen _____
Head of Department, **Electrical and Electronics Engineering**

Prof. Dr. Cengiz Beşikçi
Supervisor, **Electrical and Electronics Engineering Department, METU** _____

Examining Committee Members:

Prof. Dr. Nevzat Gençer _____
Electrical and Electronics Engineering Dept., METU

Prof. Dr. Cengiz Beşikçi _____
Electrical and Electronics Engineering Dept., METU

Assist. Prof. Dr. Haluk Külah _____
Electrical and Electronics Engineering Dept., METU

Assist. Prof. Dr. Behzat Şahin _____
Electrical and Electronics Engineering Dept., METU

Prof. Dr. Mehmet Parlak _____
Physics Dept., METU

Date: 3.9.2008

I hereby declare that all information in this document has been obtained and presented in accordance with academic rules and ethical conduct. I also declare that, as required by these rules and conduct, I have fully cited and referenced all material and results that are not original to this work.

Name, Last name : Melih Kaldırım

Signature :

ABSTRACT

DUAL AND SINGLE COLOR MID-WAVELENGTH INFRARED QUANTUM WELL PHOTODETECTORS

Kaldırım, Melih
M.Sc., Department of Electrical And Electronics Engineering
Supervisor: Prof. Dr. Cengiz Beşikçi

September 2008, 90 pages

Quantum Well Infrared Photodetector (QWIP) technology is promising for the development of large format low cost single and dual/multi color infrared sensor arrays. Thanks to the mature III-V semiconductor technology, QWIP focal plane arrays (FPAs) provide high uniformity and excellent noise equivalent temperature difference (NETD) in both long wavelength infrared (LWIR 8-12 μm) and mid wavelength infrared (MWIR 3-5 μm) bands. This thesis work focuses on the development of large format single and dual color MWIR QWIP FPAs.

For single band MWIR detection, we report QWIP FPAs on InP substrate as an alternative to the GaAs based MWIR QWIPs suffering from the degrading effects of lattice mismatched epitaxy. In the course of this work, epitaxial growth conditions of the device structure were optimized and 640×512 AlInAs/InGaAs QWIP FPAs on InP

substrate have been fabricated yielding NETD of 22 mK (f/1.5) and background limited performance (BLIP) temperature as high as 115 K

In the second part, we report the first voltage tunable 640×512 dual color MWIR QWIP FPA. After optimizing epitaxial growth of AlGaAs/InGaAs material system, we have designed and implemented the device structure to yield voltage tunable spectral response in two different windows in the MWIR band. The FPA provides NETDs of 60 and 30 mK (f/1.5) in colors 1 and 2. The results are very encouraging for the development of low cost dual/multi color FPAs since our approach utilizes one In bump per pixel allowing fabrication of dual color FPAs with the same process steps for single color FPAs.

Keywords: QWIP , Dual Color Detection, MWIR

ÖZ

ÇİFT VE TEK RENKLİ ORTA DALGABOYU KIZILÖTESİ KUANTUM KUYULU FOTODEDEKTÖRLER

Kaldırım, Melih
Yüksek Lisans., Elektrik Elektronik mühendisliği Bölümü
Tez Yürütücüsü: Prof. Dr. Cengiz Beşikçi

Eylül 2008, 90 sayfa

Kuantum Kuyulu Kızılötesi Fotodedektör (KKKF) teknolojisi geniş formatlı düşük maliyetli tek ve çift/çoklu renkli kızılötesi sensor dizinlerinin geliştirilmesi için gelecek vaat etmektedir. KKKF odak düzlem matrisleri (ODM) gelişmiş III-V yarıiletken teknolojsi sayesinde hem uzun dalgaboyu kızılötesi (UDK 8-12 μm) hem de orta dalgaboyu kızılötesi (ODK 3-5 μm) bantlarında yüksek homojenlik ve mükemmel gürültü eşdeğer sıcaklık farkı (GESF) değerleri sağlamaktadır. Bu tez çalışması geniş formatlı tek ve çift renkli ODK KKKF ODMlerin geliştirilmesine odaklanmıştır.

Tek bantlı ODK algılama için örgü uyumsuz epitaksinin performans düşürücü niteliklerinden etkilenen GaAs tabanlı ODK KKKFlere alternatif olarak InP tabanlı KKKF ODMleri sunuyoruz. Bu tez kapsamında aygıt yapısının epitaksiyel büyütme koşulları optimize edilmiş ve 22 mK GESF (f/1.5) ve 115 K kadar yüksek arka plan

sınırlı performans (APSP) sıcaklığı sunan InP tabanlı 640×512 AlInAs/InGaAs KKKF ODMler üretilmiştir.

İkinci kısımda ilk gerilim ayarlı 640×512 çift renkli ODK KKKF ODMyi sunuyoruz. AlGaAs/InGaAs malzeme sisteminin epitaksiyel büyütmesinin optimizasyonundan sonra ODK bandındaki iki ayrı pencerede gerilim ayarlı spektral tepkisellik sunan aygıt yapısını tasarımlayıp uyguladık. Bu ODM 1. ve 2. renklerde 60 ve 30 mK GESF değerlerini sağlamaktadır. Yaklaşımımız piksel başına bir In top kullanarak çift renkli ODMlerin tek renkli ODMlerle aynı işlemlerle üretilebilmesini mümkün kıldığından dolayı elde edilen sonuçlar, düşük maliyetli çift/çoklu renkli ODM geliştirilmesi için umut vericidir.

Anahtar Kelimeler: KKKF , Çift Renkli Algılama , ODK

ACKNOWLEDGEMENTS

I would like to thank my thesis advisor Prof.Dr. Cengiz Beşikçi for his guidance , supervision and providing me the possibility to work in such a sophisticated laboratory.

I would like to thank Prof.Dr.Mehmet Parlak for being on my thesis committee and allowing me to use his laboratory for the Hall effect measurements. I would like to thank also Mr. Mustafa Huş and Mr. Tahir Çolakoğlu for the Hall effect measurements.

I would like to thank Prof. Dr. Nevzat Gençer, Asst. Prof. Dr Haluk Külah and Asst. Prof. Dr. Behzat Şahin for being in my thesis committee.

I would like to thank Prof. Dr. Tayfun Akın Mr. Orhan Akar and Ms. Gözde Yaşinok for sharing their laboratories and careful dicing of our samples.

I would like to thank Dr. Oray Orkun Cellek , Dr. Selçuk Özer and Mr. Ümid Tümkaya for sharing with me their knowledge about semiconductor physics and manufacturing , for their valuable comments and opinions and their friendship. I specially thank to Mr. Ümid Tümkaya for his participation in the fabrication of focal plane arrays.

I would like to thank Mr. Burak Aşıcı for the discussions and his opinions, his efforts to help us in our work and his friendship.

I would like to express my gratitude to Mr. Süleyman Umut Eker and Mr. Yetkin Arslan for all the fruitful brainstorming that we had, for their invaluable friendship and for every moment that we have spent throughout this research. Special thanks to Mr.

Süleyman Umut Eker for staying still during extended periods of time in capturing images.

I would like to thank Mr. Hasan Koçer for all his friendship and helpful discussions.

I would like to thank Mr. Özgür Şen for the extraordinary energy and effort that he has produced in order to keep the laboratory running and for his friendship.

I would like to thank all of the past and present members of our research group for their friendship.

I would like to thank my long time friends Mr. Kartal Çağatay and Mr. Gençer Genç for all their support and friendship.

Last but not the least, I want to express my deep love and gratitude to my family for their never ending support .

TABLE OF CONTENTS

LIST OF FIGURES

FIGURES

LIST OF SYMBOLS

SYMBOLS

I_{BB}	Spectral radiant emittance at wavelength (W μm^{-1} m^{-2})
ε	Emissivity
T	Temperature (K)
h	Planck's constant (6.6256×10^{-34} J.s)
c	The speed of light in vacuum (2.998×10^{10} cm/s)
k	Boltzmann constant (1.381×10^{-23} J/K)
q	Electric charge (1.6×10^{-19} C)
λ	Wavelength (μm)
A	Area (cm^2)
η	Quantum efficiency
g	Gain of the detector
I	Current (A)
E_a	Activation energy (eV)
R	Responsivity (A/W)
f	f-number of the aperture
Δf	Electrical measurement bandwidth
D^*	Detectivity ($cm.Hz^{1/2}/W$)

CHAPTER 1

INTRODUCTION

Infrared detection technology has evolved from single element scanned systems to megapixel level, dual color imagers in the history. Throughout this progress, various "generations" of infrared detectors have been used. Single element detectors which require both horizontal and vertical scanning in order to form an image are considered as the zeroth generation.

The first generation infrared detectors are composed of one dimensional scanned arrays up to 240 detector elements. The second generation infrared detectors emerged as 240×4 scanned arrays and 2D focal plane arrays (FPAs) of low format such as 64×64. Later on the resolution of the second generation imagers have reached to 576×7 in scanned arrays and 640×512 in FPAs. Parallel to the advance in the cooled infrared detectors, uncooled systems emerged at the same time with the second generation imagers. Third generation infrared imagers are foreseen as FPAs with higher resolution, multi spectral detection and on chip signal processing capabilities. Currently third generation infrared systems are on development and they are expected to be fielded in the coming years.

Research on the quantum well infrared photodetectors (QWIPs) has started in late 1980's and nowadays the single color, large format QWIP FPAs are in production. This rapid progress in the QWIP technology is due to the mature growth and processing techniques of the III-V materials. Today QWIPs are considered as a low cost alternative to the HgCdTe detectors. Since QWIP processing technology offers higher yield and the QWIP

material can be grown with superior uniformity and reproducibility with respect to HgCdTe, on wafers as large as 6", large format QWIP FPAs can be produced at significantly lower costs and at higher resolutions. As a result, while the high end applications which need very long range performance are dominated by HgCdTe scanned systems and uncooled micro-bolometers are used widely in the low end systems because of their very low cost, QWIP imagers are used in mid end applications. These applications need moderate range performance and high resolution for better target identification, alongside with lower cost. Currently there is no other technology than QWIP, offering large format photon detectors at an affordable price. QWIPs also pose an advantage in multi-spectral detection as will be covered in the coming sections.

The materials used in QWIP devices can be various combinations of III-V materials. The most commonly used technology is the $Al_xGa_{1-x}As/GaAs$ technology. $Al_xGa_{1-x}As/GaAs$ material system is lattice matched to GaAs substrates and long wavelength infrared (LWIR) sensors can be produced using this heterostructure. This technology benefits from the GaAs technology which can be considered as the most mature one after Silicon. MWIR detection can be realized by employing strained layers of $In_yGa_{1-y}As$ for the quantum wells. Another technology important for the QWIP growth is the InP technology. Growth and processing of InP structures are almost equally mature as GaAs and 4" InP substrates are available commercially. InP based LWIR QWIPs are manufactured using $InP/In_{0.53}Ga_{0.47}As$ or $InP/Ga_xIn_{1-x}As_yP_{1-y}$ material systems lattice matched to InP. These devices offer significantly higher responsivity compared to the $Al_xGa_{1-x}As/GaAs$ material system [1, 2]. Also InP based QWIPs in the MWIR band are possible using $In_{0.52}Al_{0.48}As/\ In_{0.53}Ga_{0.47}As$ heterostructures. These MWIR devices can be grown lattice matched to InP substrates, removing the limitations of strained layer epitaxy. By the use of the above structures QWIPs can provide detection in both LWIR and MWIR spectral bands, which is expected from a material system to be used in third generation infrared imagers.

Third generation systems are desired to perform dual/multi spectral imaging. Dual/multi spectral imaging may include obtaining images in LWIR and MWIR bands (separately) with one FPA (dual band) or in different wavelength regions in either band (dual color). Also imaging in more than two spectral windows is possible, leading to multi band/multi color imaging. Dual/multi spectral imaging is capable of remotely determining the absolute temperature of the object in scene. Also dual/multi spectral sensors provide better imaging in the presence of countermeasures, camouflage, background clutter and they can be used to determine infrared signatures of certain targets. Dual/multi spectral sensors with the above mentioned capabilities enhance infrared vision to a point where single color sensors can not approach whatever their sensitivity is.

QWIPs have certain advantages over HgCdTe sensors in dual/multi spectral imaging. First the QWIP detection spectrum can be tuned in a wide range more precisely compared to HgCdTe sensors. Also QWIP detectors sense infrared radiation in a narrow spectrum and this property of QWIPs provide substantially less spectral crosstalk than HgCdTe sensors. QWIPs can also be coupled with interband detectors of III-V materials which can sense in short wave infrared (SWIR) band to observe laser designators and range finders.

QWIP FPAs having dual/multi spectral imaging capability can be fabricated by two approaches. The first approach has three contacts per pixel. Data of each color is read from one contact while the third contact serves as the common contact. By this method the information of two colors is obtained simultaneously. The second method is switching the detection spectrum of the sensor by the applied voltage. The dual/multi spectral image can be formed by alternating the bias on the detector for consecutive frames. This voltage switchable approach permits use of one contact per pixel for signal reading, while the common contact is same for all pixels and obtained from a separate part of the FPA away from the pixels.

The fabrication of the voltage switchable FPAs is totally same as the single color array fabrication, thus the voltage switchable FPAs can be produced right away with no further optimization of fabrication processes. On the other hand, three contact FPAs require a development phase to go into production because of changes needed in fabrication. Furthermore, vias must be fabricated to obtain three contacts per pixel. This decreases the fill factor and restricts the pixel size. Also the cost may increase due to decreasing yield of a more complex process. The restriction of pixel size results in restriction of the fill factor of the detector array. As a result, while voltage switchable FPAs can be extended to megapixel arrays in an easy and inexpensive way, currently no three contact FPA larger than 384×288 format is reported. Obtaining larger sized arrays seems to be very difficult due to pixel size limitations.

As discussed above, dual/multi spectral imaging may include detection at various wavelengths. One of these applications is the MWIR/MWIR dual color imaging. These detectors may be used for determination of certain infrared signatures (such as CO_2 plumes), eliminating the reflection or scattering effects of the Sun while looking at hot objects and discrimination of countermeasures.

During this thesis work, development of the GaAs based voltage tunable dual color MWIR/MWIR QWIP FPAs and the InP based single band MWIR QWIP FPAs is accomplished. The work includes epitaxial growth of the QWIP device using molecular beam epitaxy (MBE), characterization of the grown material and characterization of the fabricated detectors at the pixel and FPA levels. At the beginning of the work the growth conditions of the epitaxial layers was optimized. Afterwards, various layers were grown and characterized to find the structure with best switching characteristics and highest performance. Lastly, performances of the FPAs which are fabricated using the optimized material by our research group were measured.

In the second chapter of the thesis, the basics of infrared detection and the infrared detector types are discussed. Also important figures of merit for an infrared detector are explained.
The third chapter includes a discussion on the operation and fabrication of QWIP and quantum dot infrared (QDIP) devices together with a survey on the present status of the QWIP technology

Fourth chapter is dedicated to the fabrication and characterization of InP based MWIR QWIP FPA. In this chapter optimization of growth of the structure and the FPA characteristics are given.

In the fifth chapter, the voltage tunable dual color MWIR/MWIR QWIP FPA is investigated. This chapter includes a discussion on the advantages and use of dual color detection, the details of the growth of the structure and lastly the performance assessment of the FPA

Sixth chapter includes conclusions and the further work that can be done.

CHAPTER 2

BASICS OF INFRARED DETECTION

Infrared imagers rely on radiation emitted by the objects, unlike the visible imagers which detect the light reflected by the objects. The performance of an infrared detector is dependent on the response given to unit illumination and the noise level of the detector. Furthermore, the detection wavelength has considerable effect on the performance since the number of the photons emitted from objects as well as the transmittance of the atmosphere varies with the wavelength.

Different approaches and materials have been used for infrared detection since the emergence of the infrared imagers. These technologies include uncooled sensor arrays, low bandgap semiconductors, type II superlattices, QWIPs and the others. Although the QWIP technology is relatively new, it has achieved maturity in short time and currently large format QWIP FPAs are produced.

In this chapter, first the basics of infrared emission and atmospheric transmission are discussed. Afterwards, different types of infrared detectors are presented. Later, the figures of merit of infrared detectors are explained.

2.1 Infrared Radiation and Thermal Imaging Principles

According to the Planck's radiation law, every object having temperature above zero Kelvin emits radiation in the form of photons. The distribution of these photons with wavelength and temperature of the object is given by the Planck distribution

$$I_{BB}(\lambda,T) = \frac{2hc^2}{\lambda^5}\frac{1}{e^{hc/\lambda kT}-1} \quad (1)$$

where λ is the wavelength of radiation and T is the temperature of the blackbody [3]. An object under radiation may absorb or reflect this radiation in addition to emitting photons. An ideal blackbody is defined as an object which absorbs all the radiation falling on it, without reflection. If a blackbody is in thermal equilibrium with its surroundings, the blackbody must also emit radiation in equal amount to that it absorbs. Thus the emissivity (ε) of the blackbody is 1.

Other objects having non-reflective surfaces may have different emissivity values depending on the wavelength of the emitted radiation or angle. For these objects emissivity is defined as a function of the angle of observation and wavelength $\varepsilon(\lambda,\phi)$. The objects having emissivity values independent of the wavelength or angle are named as "grey bodies" with a certain emissivity value. The total radiation emitted by an object is given as the emissivity of the object multiplied by the Planck distribution.

In Figure 1, the Planck distribution is plotted as a function of wavelength for various object temperatures. As it can be seen from this figure, for the objects at 300 K the Planck distribution peaks at 10 μm wavelength which is in the infrared region of the electromagnetic spectrum. Infrared detectors provide a means to see the objects at absolute darkness by detecting this radiation. This is the basis for the thermal imaging systems that use infrared detectors as the core.

Though the objects radiate infrared photons, these photons must propagate through the atmosphere in order to reach the imaging system. However atmospheric gases can absorb these photons. These gases include H_2O, CO2, CH_4, N_2O, O_3 and many more. The dominant ones are H_2O and CO_2 at low altitudes. The absorption of H_2O (water vapor) is one of the main factors affecting the performance of infrared systems, since the concentration of the water vapor is quite variant depending on the geographical condition and weather. Also in marine applications, the water vapor absorption is more prominent with respect to land applications. As a result of the absorption of atmospheric gases, certain bands in the infrared region are formed. The atmospheric transmission regions are given in Figure 2.

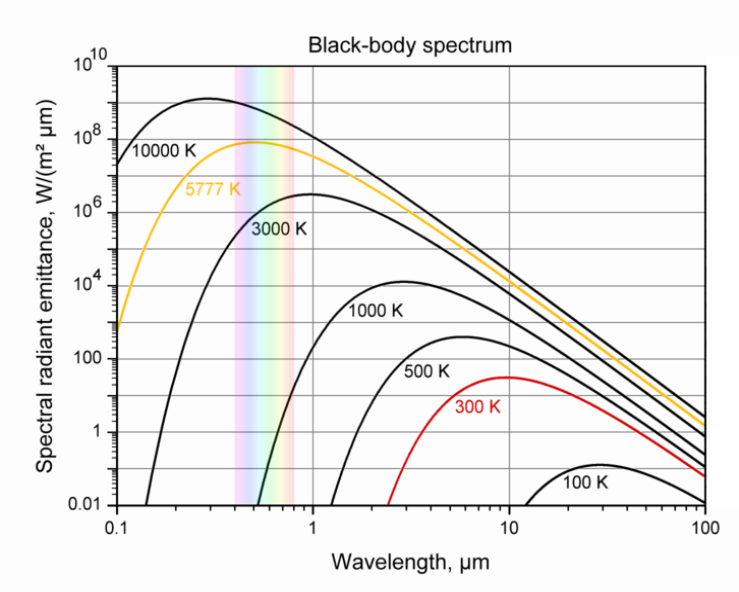

Figure 1: The spectral emittance of a blackbody source versus wavelength [4]

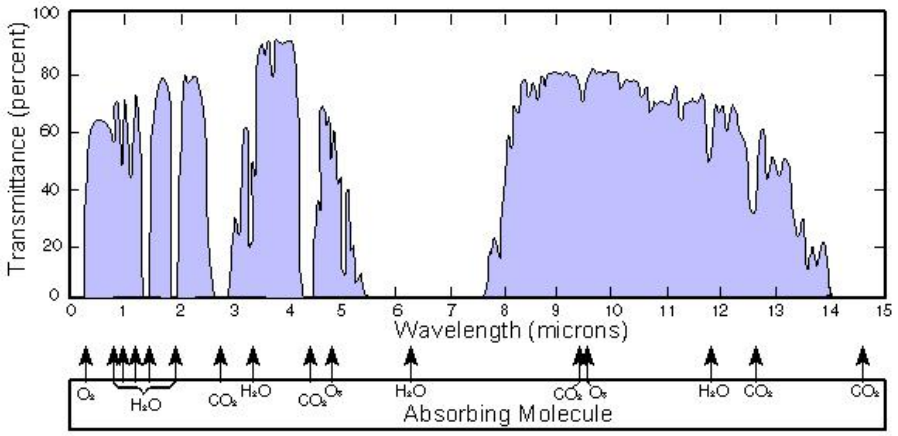

Figure 2: The atmospheric transmission of radiation versus wavelength in the infrared region. The gas molecules responsible for absorption are also depicted in the figure. [5]

In this transmission diagram, the region between 8 μm and 14 μm is called the long wavelength infrared (LWIR) region. There is another window of transmission between 3 μm and 5 μm which is called the mid-wavelength infrared (MWIR) region. Note that, in the MWIR region there is a dead region around 4.2 μm resulting from the CO_2 absorption. The region below 3 μm up to the visible region includes the short wavelength infrared (SWIR) region and near infrared (NIR) regions situated at 1.4 μm-3 μm and 0.75 μm-1.4 μm intervals, respectively. Among these bands MWIR and LWIR bands are suitable for thermal imaging as they contain sufficiently high number of photons for near room temperature objects. SWIR and NIR band imaging is mostly due to the reflected photons from the objects like visible imaging.

Another issue is the scattering of the light due to aerosol particles. This phenomenon occurs most often in dusty or foggy weather. Since the amount of scattering is inversely proportional to the wavelength of radiation, infrared detectors which are sensitive to

longer wavelengths with respect to visible light is advantageous also in the above conditions

A typical infrared imaging system consists of a detector, a cold stop to define the field of view of the detector, a lens to form the image on the detector (which has the same field of view with the cold stop) and imaging electronics that drive the detector and acquire data from the detector. In addition to these, systems using cooled detectors utilize closed cycle coolers to operate the detectors at cryogenic temperatures. These detectors are mounted in vacuumed dewars in order to preserve cryogenic environment and to prevent condensation on detector. On the other hand, uncooled detectors are vacuum packaged and mounted to thermoelectric modules to keep the temperature of the detector constant [6].

For an imaging system, the total optical power falling on the unit area of a detector from a background which is having temperature T is given as:

$$P_{opt} = \frac{1}{4f^2 + 1} I_{BB}(T) \tag{2}$$

where f is the f-number of detector, which is described as the ratio of the distance between optical aperture of the cold stop and detector, to the diameter of aperture. $I_{BB}(T)$ is the total emittance of the background.

Infrared imaging has been an important field of research since it offers many areas of application in both military and civilian. The military applications range from night vision devices to heat seeker missiles. The civilian applications can be listed as search and rescue operations, biomedical imaging, process control, fault detection in industry and many more.

2.2 Types of Infrared Detectors

Infrared detectors can be described generally as transducers converting the infrared photons to electrical signals. In order to accomplish this conversion various physical phenomena may be used. A detector may use the direct interaction of electrons and photons as well as the heating effects caused by absorbed energy to detect the radiation. By this difference the infrared detectors are divided in two main subgroups:

1) Photon detectors
2) Thermal detectors

Photon detectors utilize the interactions of the charge carriers and photons. The basis of detection is the transition of carriers to different energy levels by absorbing the photon, resulting in change in the current passing through the structure. Photon detectors are sensitive to definite wavelengths of the infrared spectrum depending on the type of transition and the energy gap between the electronic states.

Thermal detectors work by measuring the change in the physical properties of materials due to heating by the absorbed photons. Micro-bolometer type detectors use the change in the resistance of a substance due to heating. They are usually formed by an absorber material isolated from the other parts of the device by suspension. This material is chosen specifically so that, its resistance changes strongly with temperature. When heated, the resistance of the absorber changes and this change is read electrically.

Pyroelectric detectors benefit from the change in the polarization of the structure. A net charge forms on the detector surfaces as a result of heating. This excess charge can be read by circuitry Thermopiles are formed of thermocouples which produces a voltage upon heating. The thermocouples are connected in series to increase the voltage produced.

The common property of the thermal detectors is their insensitivity to the wavelength of the photons impinging on the detector. Though the optics or material properties may put a limit on the absorption, by design the detectors are sensitive solely to the power of the radiation. Among these detectors, micro-bolometers give the best performance.

The different detection scheme utilized in photon and thermal detectors results in a fundamental difference in the operation between these two kinds of detectors. The photon detectors must be cooled to cryogenic temperatures in order to suppress the thermal activation of the electrons. The need for the expensive cryo-cooling equipment of photon detectors constitutes a significant portion of the price of the system increasing the cost as well as the power consumption. On the other hand the thermal detectors need not to be cooled. In addition the thermal detectors, especially micro-bolometers, can be fabricated using Silicon material which has significantly lower fabrication cost compared to the compound semiconductors commonly used in fabrication of photon detectors. Although the photon detectors need cryogenic cooling, once they are cooled, their sensitivity exceeds the thermal detectors and they can operate at higher frame rates. The thermal detectors are restricted to lower frame rates, because the detector performance is limited by the thermal time constant of pixels. If this time constant is lowered, signal to noise ratio decreases. In addition, realizing dual/multi spectral imaging with uncooled detectors is not possible. The lack of discriminating between the different bands in infrared makes the thermal detectors more prone to clutter and decreases the performance in high temperature backgrounds.

The differences stated above, result in the separation of the applications of photon and thermal detectors. Thermal detectors are used for applications that need low cost and low power such as portable devices or civilian use that usually does not need very high performance. On the other hand, the photon detectors are used for mainly military and medical applications and in locations where the power requirements can be fulfilled.

The photon detectors are also divided into subgroups. The first group is the photovoltaic detectors in which built in electric fields of structure is used for collecting the excited carriers. The most common example is the p-n junction photodiodes although devices based on asymmetric quantum wells have been demonstrated [7]. The photoconductors are biased using a bias source outside the detector and thus the collection of charge carriers is facilitated.

In the infrared region the materials used commonly for the fabrication of photon detectors can be listed as low bandgap semiconductor materials, QWIP structures and type II strained layer superlattices (SLSs). Also there are other types of photon detectors investigated.

InSb and $Hg_xCd_{1-x}Te$ are the most commonly used low bandgap materials in the infrared region. Since InSb is a binary compound, its bandgap is fixed and it can only be used in MWIR region. This leaves InSb material out of the possibilities for realizing multi spectral detection. $Hg_xCd_{1-x}Te$ is a ternary II-VI compound whose bandgap can be tuned to SWIR, MWIR or LWIR by changing the composition. $Hg_xCd_{1-x}Te$ can be used for fabrication of dual color or dual band detectors with high performance. However the complications included in the growth and fabrication of the material decreases the yield of fabrication resulting in high cost. First of the difficulties associated with the material is the lack of large area lattice matched substrates. For lattice matched growth of $Hg_xCd1_{-x}Te$ material CdZnTe substrates are used. CdZnTe substrates, 7cmx7cm in size have been demonstrated [8]. However the substrates commercially available are not at the half area of these. The $Hg_xCd_{1-x}Te$ layers grown on lattice mismatched GaAs, Si or Ge substrates usually have higher defect density compared to the ones on CdZnTe. Another problem of $Hg_xCd_{1-x}Te$ material is the high non-uniformity. This non-uniformity is a result of very strong dependence of the material bandgap on the composition especially for the bandgap values corresponding to the LWIR band. Also the material

composition is highly dependant on growth conditions and hard to control. The processing of grown layers is also problematic, because of the low mechanical strength of the material and low resistance to high temperatures. Because of these problems various alternative infrared detector materials are investigated.

QWIP devices are composed of multi quantum well (MQW) layers fabricated using alternating layers of III-V semiconductors. As a result of this, they benefit from the mature material growth and processing technology developed for production of telecommunication devices. The conduction band edge profile of a QWIP device can be seen in Figure 3. The compound having lower bandgap constitutes the quantum well while the compound with larger bandgap forms the barrier. Energy states are formed inside the quantum well as a result of confinement of electrons. The operation of the device is based on excitation of the electrons from the bound states to the higher energy states by absorbing photons. While the electrons do not contribute to conduction in bound states, when they are excited they can be transported outside the well regions participating in conduction and increasing the current through the device. The details of QWIP operation and related devices such as quantum dot infrared photodetector (QDIP) will be discussed in the next chapter.

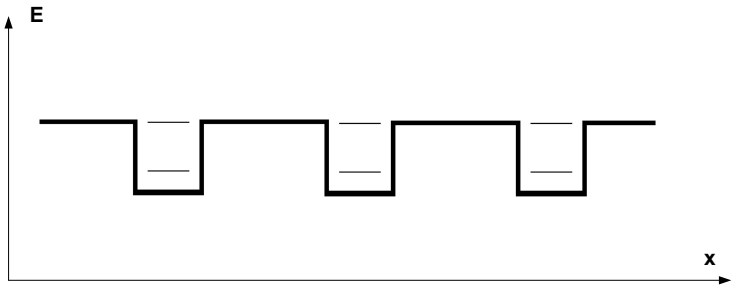

Figure 3: The conduction band edge diagram of QWIP structure. The thin lines inside the wells represent discrete energy states formed as a result of quantum confinement.

Recently type II SLS structures based on InAs/GaSb or InAs/GaInSb material system has emerged as an alternative in infrared detection. The band structure of this system can be seen in Figure 4. In this material system, the valence band of GaSb material is aligned with conduction band of InAs, forming a low energy gap. By tuning the structure, this bandgap can be adjusted for detection in MWIR and LWIR bands. Type II SLS structures give quantum efficiency values close to $Hg_xCd_{1-x}Te$ material and they have better uniformity compared to $Hg_xCd_{1-x}Te$. The growth and processing of these structures are complicated with respect to QWIP and passivation of devices operating at LWIR band is problematic. Although they possess a potential, the type II SLS structures are still in the research phase for production of third generation infrared imagers.

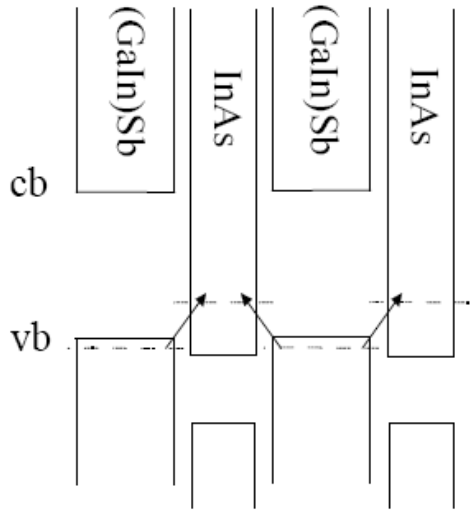

Figure 4: The band structure of type II SLS structures [9].

The other kinds of photon detectors include PtSi Schottky diodes which work in MWIR region and extrinsic photoconductors such as Ge:Hg. Extrinsic photoconductors were used in the very beginning of the infrared imaging and are no longer considered since

they need to be cooled down to extremely low temperatures. PtSi detectors have the advantage to be manufactured on silicon however they suffer from very low quantum efficiency (~1%).

Among these detector types $Hg_xCd_{1-x}Te$ detectors are expected to dominate the high end market with improvements in the growth and manufacturing technology. Readout integrated circuit (ROIC) technology also plays a role on the performance of IR sensors. Currently, the limitations of ROIC integration capacitances limit the infrared detector performance [10]. Since for an FPA working at background limited infrared performance (BLIP) condition, integration time is limited by the photocurrent injected, $Hg_xCd_{1-x}Te$ detectors having higher photocurrent due to their higher quantum efficiency, use shorter integration times with respect to QWIPs. This leads to an increase in the noise bandwidth and increases NETD. Furthermore, the non-uniformity of $Hg_xCd_{1-x}Te$ arrays can be limiting on the performance. QWIP devices therefore are not very far from $Hg_xCd_{1-x}Te$ detectors in terms of imaging performance. The growth and fabrication techniques of QWIP are highly mature compared to both $Hg_xCd_{1-x}Te$ and type II SLS detectors and decreases the cost per FPA. Combining these advantages with the ease of fabrication in the dual/multi color structures, QWIP devices can be considered as a strong alternative for future of infrared detection.

2.3 Infrared Detector Figures of Merit

To assess the performance of infrared detectors, one must, for sure, evaluate how much signal is generated by unit illumination power and the level of noise of the detector. Also the amount of change in the radiation with the change in target temperature is needed to find the sensitivity of the detector. By combining these parameters with the system related parameters like the f-number or window transmission, the minimum change in

the temperature that the detector can sense can be determined. These figures of merit can be listed as:

1) Responsivity which is the measure of detector's response to unit illumination,

2) Noise,

3) Detectivity which is the inverse of noise equivalent power normalized to detector area and measurement bandwidth,

4) Noise equivalent temperature difference (NETD), which is the temperature sensitivity of one sensor.

These parameters will be discussed briefly in this section.

Responsivity:

Responsivity is the rate of change in the detector signal with the optical power falling on the detector. For the photon detectors, the measured signal is the current through the detector Responsivity is expressed as:

$$R = q\eta g \quad \text{(A/ photon second)} \tag{3}$$

where q is the electronic charge, η is called absorption quantum efficiency and g is called photoconductive gain [3]. The absorption quantum efficiency is the probability of absorption of a photon that is incident on the detector. It is dependent on the density of carriers available for excitation, total thickness of the detector material and the probability of interaction between electrons ad photons. Photoconductive gain is the proportion of excited carriers (i.e. absorbed photons) to the carriers collected by the readout device. While g is ~1 for photovoltaic devices, its value is variable for photoconductors and is determined by L_d/L where L_d is the average drift distance of electrons and L is the device length. To convert the responsivity expression from photon to the power terms we divide the expression with the energy carried by a photon to obtain the expression:

$$R = q\eta g \frac{\lambda_d}{hc} \text{ (A/W)} \quad (4)$$

where λ_d is the wavelength of the detected photon, h is the Planck constant and c is the speed of light in vacuum.

Noise

Although the responsivity determines the signal level, it is not sufficient to estimate the performance without knowledge of the noise generated by the device. There are several mechanisms for generation of noise in photon detectors. These are namely shot noise, generation-recombination (GR) noise, 1/f noise and Johnson noise. Of these noise mechanisms the ones that are particularly important are the shot noise and GR noise, Shot noise is the noise resulting from the random arrival of the photons and it depicts the lowest noise level achievable by a detector. If the detector temperature is low enough to overcome the Johnson noise, GR noise is the dominant mechanism in photoconductive detectors including the QWIPs. The relations for the shot noise and GR noise currents are given as:

$$i_n^2 = 2qI_{avg}\Delta f \quad (5)$$

$$i_n^2 = 4qg_{noise}I_{avg}\Delta f \quad (6)$$

respectively where Δf is the measurement bandwidth and g_{noise} is the noise gain [3]. Under low biases where the impact ionization is not occurring, the noise gain is assumed to be same with the photoconductive gain for QWIPs [11,12].

An infrared detector would unavoidably have current flowing through it without any illumination if there is any bias on the detector. This current is called the “dark current” of the detector and this current also creates noise. Dark current is usually more prominent in photoconductors since they are used at high biases compared to the photovoltaic

detectors which are used at zero or very low bias levels. By considering dark current and photocurrent separately, resulting noise expression becomes:

$$i_n^2 = 4qg_{noise}\,(I_{photo}+I_{dark})\Delta f \qquad (7)$$

Thus the noise has two components, one due to photocurrent and the other due to dark current. If the noise of a detector is limited by the noise which is generated by the photocurrent rather then the dark current, the detector is said to achieve "background limited performance" (BLIP) condition. For BLIP operation $I_{photo} >> I_{dark}$ condition must be satisfied.

Detectivity

Knowing the signal and noise levels one can calculate the optical power needed to generate a signal which is equal to the noise level. This power is called the "noise equivalent power" (NEP), and it is expressed as

$$NEP = \frac{i_n}{R} \qquad (8)$$

Detectivity is defined as the inverse of NEP. Specific detectivity denoted with D^* is the detectivity normalized to the detector area and the measurement bandwidth. However, since specific detectivity is used much more frequently than the detectivity, from this point simply detectivity term will be used for the specific detectivity. The expression for detectivity is:

$$D^* = \frac{\sqrt{A\Delta f}\,R}{i_n} \qquad (9)$$

where A is the detector active area [3]. Since i_n^2 is directly proportional to bandwidth and detector area (because of the total current), the normalization is done with the square roots of these parameters. By this way the detector performance is evaluated independent of area and bandwidth.

If we assume a photoconductive detector under BLIP condition, we can calculate I_{photo} by multiplying equation 2 by equation 4 and the detector area to obtain:

$$I_{photo} = qA\frac{1}{4f^2+1} I_{BB}\eta g \frac{\lambda_d}{hc} \tag{10}$$

Using this expression, the noise current under BLIP condition can be calculated by neglecting the I_{dark} term in equation 7 and replacing I_{photo} by equation 10. Furthermore, by assuming $g=g_{noise}$ and putting in the noise current obtained and equation 4 in equation 9, we obtain the BLIP D^* expression as

$$D^*_{BLIP} = \frac{\sqrt{\eta\lambda_d(4f^2+1)}}{2\sqrt{hcI_{BB}}} \text{ cm}\sqrt{\text{Hz}}/\text{W} \tag{11}$$

As it can be seen in equation 11, D^*_{BLIP} is increases with the f-number of the optics as long as the detector stays BLIP.

When discussing of parameters R and D^*, one should bear in mind that these parameters change with the wavelength. Therefore, they may be expressed as $R(\lambda)$ and $D^*(\lambda)$.

Noise Equivalent Temperature Difference (NETD)

To assess the performance of an imaging system, the minimum temperature difference on the target which can be resolved from the noise in the infrared images is determined. NETD is a parameter of the FPA which includes the information of imaging band, the detectivity and the total amount of radiation received.

Starting from NEP, NETD can be determined by dividing the NEP expression to derivative of the total optical power received by the detector with respect to the target temperature [3]. If we express the NEP in terms of detectivity as

$$NEP = \frac{\sqrt{A\Delta f}}{D^*} \tag{11}$$

The derivative of the received optical power by the detector with respect to the target temperature can be expressed as follows if the target is assumed to be a blackbody.

$$M_{BB} = A\frac{1}{4f^2+1}\frac{dI_{BB}}{dT} \tag{12}$$

By dividing expression 11 with expression 12 we can find the NETD of detector. Also since D^* and M_{BB} are dependent on the wavelength of radiation, their multiplication is replaced by an integral resulting in

$$NETD = \frac{(4f^2+1)\sqrt{\Delta f}}{\sqrt{A}\int D^* \frac{dI_{BB}}{dT}dT} \tag{13}$$

Note that for a detector under BLIP condition, since D^* is proportional to $\sqrt{(4f^2+1)}$ NETD will be dependant on $\sqrt{(4f^2+1)}$ too. However in dark current limited case, since the noise current is independent of the *f*-number, D^* will not have a dependency on this parameter leaving the NETD changing with $(4f^2+1)$. During the calculation of NETD values, the background temperature, is usually taken to be 300 K .

In the next chapter, the basics of the operation and fabrication of the QWIP and QDIP devices will be explained and information about the current status of the QWIP and QDIP technology will be presented.

CHAPTER 3

QUANTUM WELL AND QUANTUM DOT INFRARED PHOTODETECTORS

Since the introduction of the QWIPs, significant amount of work has been performed to investigate and improve the performance of these structures. Different type of structures and material systems were offered to modify the electrical properties as well as different approaches in fabrication to increase light coupling. Recently, quantum dot infrared photodetector (QDIP) structures have been introduced as an alternative.

The key parameters that require investigation is dark current, detection spectrum, the quantum efficiency and the gain of the structure. If we have the knowledge of these parameters, the device responsivity, detectivity and NETD can be estimated. QWIP differs from the conventional photoconductors by the mechanism of electron photon interaction as well as the transport properties of electrons in the structure. To assess the device operation and modify the characteristics when needed, one should have information about these parameters.

3.1 Structure and Operation of QWIP and QDIP

The basis of operation for both QWIP and QDIP is the intersubband transition concept which was briefly explained in section 2.2. If the intersubband transition in QWIPs is investigated in detail, it is seen that there are different types of QWIP devices, based on

the position of the excited energy level with respect to the edge of the energy barrier. These types are illustrated in Figure 5. The bound to bound QWIP device has the excited state energy lower than the height of the barrier. In this device the electrons tunnel through the barrier to join the current flow. With bias applied to the structure, the barriers lower leaving a thinner cross section for the electrons to tunnel. The bound to quasi-bound QWIP has the excited state level with the edge of the barrier while in the bound to continuum device the electrons are excited to continuum states above the barrier. In addition to these structures, devices that employ thin barriers between quantum wells are also investigated. In these structures minibands are formed inside the superlattice and electrons are transferred in between these minibands resulting in broader absorption spectra.

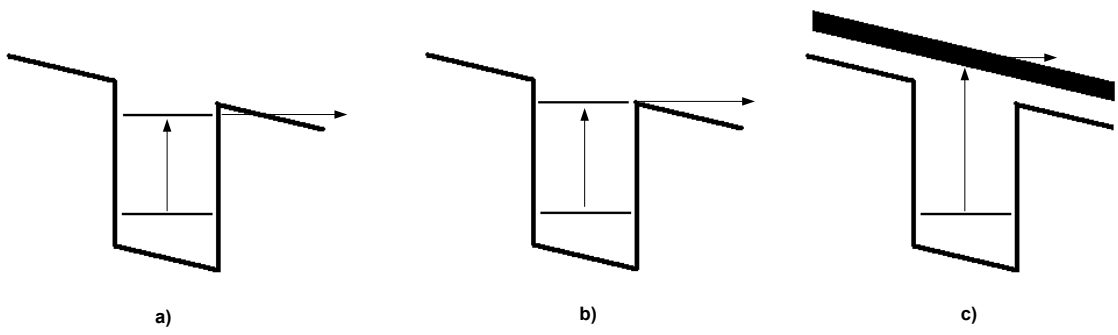

Figure 5 : Conduction band edge profiles of different types of QWIPs. a) bound to bound b) bound to quasibound and c) bound to continuum.

QDIP devices differ from QWIPs by the usage of three dimensional confinement of the electrons. QDIPs are realized by self assembly of quantum dots during epitaxial growth of layers having high lattice mismatch. Disk shaped quantum dots which are formed, accompanied by a very thin wetting layer in this process can be seen in Figure 6. In

QDIP, the excitation of electrons is from the states inside the quantum well to the conduction states.

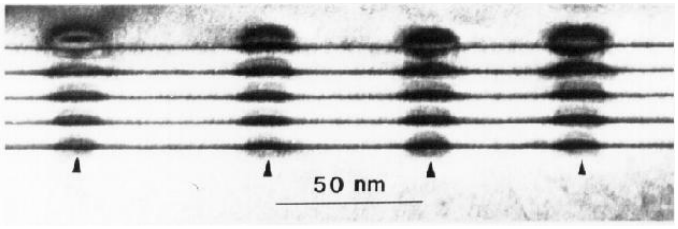

Figure 6: Cross sectional transmission electron microscope image of InAs quantum dots grown epitaxially on GaAs [13].

In addition to the QDIP devices, there exists a modified version of QDIP called dots-in-well (DWELL) detector. In DWELL QDIPs the quantum dot material is placed inside a quantum well. The energy band profile of this device can be seen in Figure 7 a. In DWELL detectors electron transitions to states that are inside the quantum well are also possible. The electrons transferred into these states, can contribute to current under bias since the quantum well is shallow. This mechanism is shown in Figure 7 b.

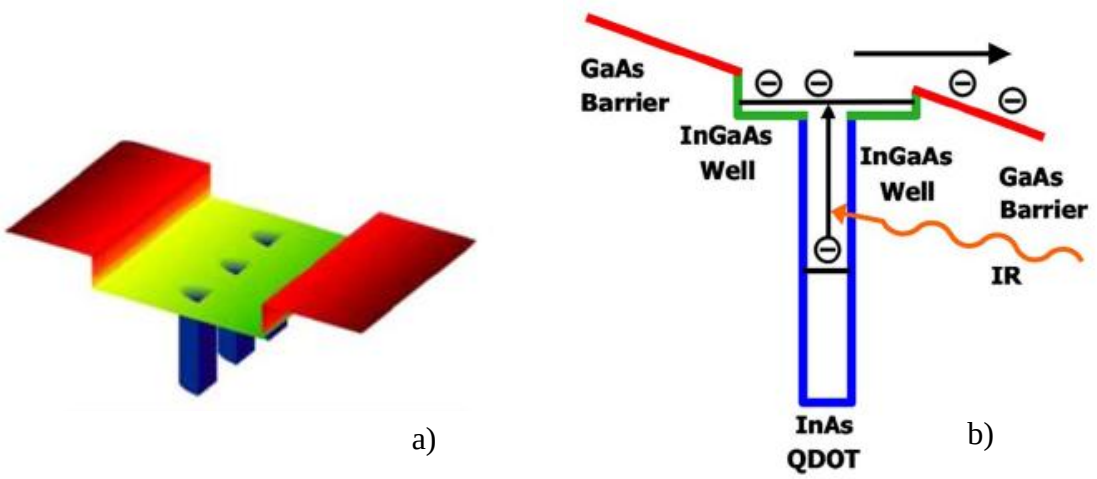

Figure 7: Conduction band edge energy profile of DWELL device (a) and excitation mechanism in DWELL QDIPs (b) [14].

The first of the important properties of the QWIP and QDIP detectors is the detection spectrum. The detection spectrum of a QWIP device is defined by the energy gap of the intersubband transitions from the ground state to the excited states. To adjust the detection wavelengths, one can change the well width and well depth. While well width is determined by the thickness of growth, the depth of the well is determined by the conduction band discontinuity between the well and barrier material. Knowing these parameters and material parameters such as effective mass of carriers, the position of the subband states can be found by solving Schrödinger equation [3]. Although some rules of thumb can be set to adjust the detection spectrum, usually it is difficult to estimate this spectrum without simulations. We can say that if the depth of the well increased, the absorption spectrum will shift to shorter wavelengths with higher energy transitions. Also the spectra are likely to have larger full width at half maximum (FWHM) in bound to continuum devices with respect to the bound to bound devices as a result of larger number of states in the continuum. The QWIP devices change from bound to bound

nature to bound to continuum nature as the width of the quantum wells is decreased. This may be explained as a result of Heisenberg uncertainty relation.

In QDIPs the detection spectrum is determined by the transitions from the states inside the quantum dot to either continuum, or spacer (quantum well) states. As quantum wells can be conceived as artificial atoms, atom-like levels are formed inside the quantum dots [15]. Since these levels are more separated from each other with respect to the levels in QWIPs, a broadening in the QDIP spectrum is observed. The QDIP detection spectrum can be controlled by changing the size of the quantum dots or the conduction band discontinuity between the dot material and the material surrounding the dot. Moreover, doping has also an effect in the detection spectrum since higher energy levels in the quantum dot can be filled or empty depending on the doping. As the doping increase, an increase in higher wavelength response is expected due to population of levels which are closer to the continuum. In DWELL detectors, the use of quantum well adds another degree of freedom to the tuning of spectrum. By changing the well width, the position of the states inside the well can be tuned in a wide range. By this way better control over spectral response is gained [16].

The effectiveness of the intersubband transitions defines the value of absorption quantum efficiency (η) of the structure. The quantum efficiency is dependant on the number of confined carriers, the oscillator strength (overlap of the wavefunctions of the excited and ground state) and the angle of incidence to the QWIP. The dependence of the absorption to the angle of incidence is a property special to the QWIP devices. Since the momentum in the quantum well plane is conserved in intersubband transitions, light having electric field parallel to this plane is not observed [3]. The absorption of light is proportional to $\sin^2(\theta)/\cos(\theta)$ where θ is the angle of incidence of the light to the QWIP surface. Unfortunately, for an FPA the light will be incident with $\theta=0°$ (perpendicular to the

surface) leading to minimum absorption. To overcome this issue, various light coupling schemes have been offered.

For the simple test structures 45° facet coupling is used. This method is illustrated in Figure 8. In this method the light is coupled to QWIP through 45° cut and polished edge of the substrate. When the light is incident with 45° to the structure, half of the light is incident parallel to the well planes giving maximum absorption.

However, this method is not applicable to FPAs. For the light coupling to FPA pixels, either diffraction gratings or corrugated pixels are used. Diffraction gratings diffract the incoming light, which is incident perpendicular to QWIP surface, in various directions to change the angle of the light propagation with respect to the quantum well plane. In this way the quantum efficiency of the device is increased. For the optimum coupling of the gratings, the period of structures is tuned to about half and depth of etch is tuned to one fourth of QWIP detection wavelength, where wavelength is considered inside the semiconductor structure [3]. Some examples of diffraction gratings are given in Figure 9 for LWIR and MWIR bands. Note that in the MWIR band the period goes down to ~1μm which decreases the minimum feature size to ~0.5 μm making the fabrication of gratings very difficult if not impossible with contact photolithography

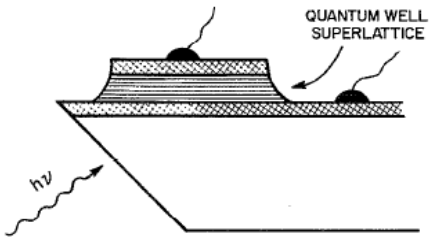

Figure 8: The 45° facet coupling configuration as illustrated by Levine [17].

a) b)

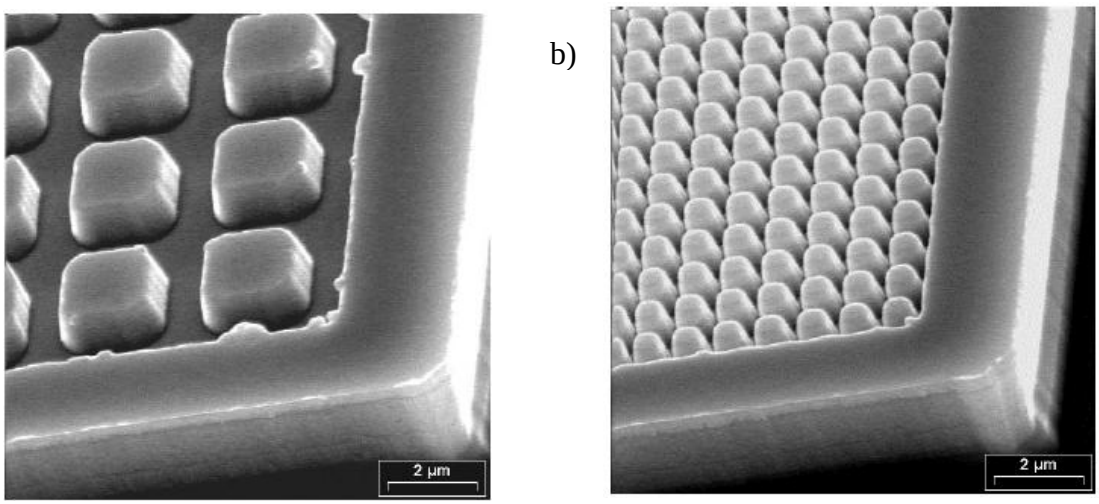

Figure 9: Two grating structures optimized for a) LWIR and b) MWIR operation [18].

Instead of gratings, the corrugated structure is also used which is depicted in Figure 10. In this structure mesa structures are etched with anisotropic enchants to form corrugations. These corrugations reflect the light into QWIP structure and change the direction of propagation. Corrugated structures have the advantage of light coupling relatively independent of wavelength, if the entire pixels are fabricated as one big corrugation instead of many small ones (Figure 10 c) [19]. This property can be useful in fabrication of multi band detectors. Small corrugations as seen in Figure 10 b, has a wavelength dependant effect like diffraction gratings.

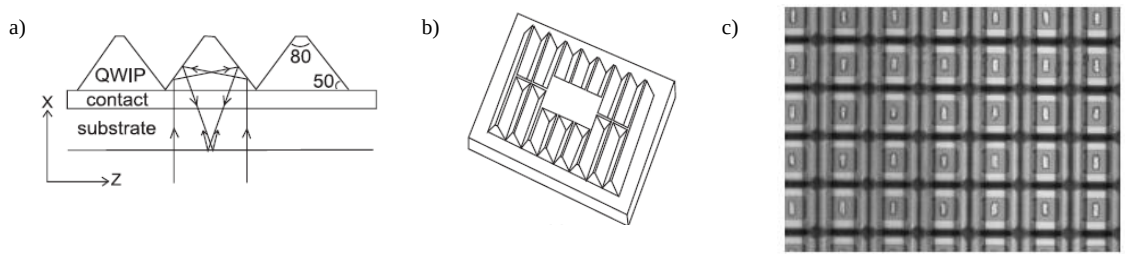

Figure 10: The principle of light coupling with corrugations a), a corrugated FPA pixel proposal with small corrugations b) [20] and optical microscope image of FPA pixels fabricated as one large corrugation c) [21]

QDIP detectors, having three dimensional confinement, were expected to perform polarization independent detection. However, QDIPs also exhibit higher absorption for the light incident perpendicular to growth direction. This is thought to be an outcome of the weaker confinement in the growth plane. This weakness is a result of the large size of quantum dots in growth plane with respect to their size in the growth direction and the presence of a wetting layer [3]. Although QDIPs can absorb perpendicularly incident photons, diffraction gratings are used in FPA fabrication to increase light coupling. QDIP detectors which are examined in the literature generally have lower quantum efficiency than the QWIPs. This is a result of the lower density of the active material (quantum dots).

Another parameter that affects the QWIP performance is the photoconductive gain of the device. Liu and coworkers have developed a model for the photoconductive gain of QWIP devices [21, 22]. The model determines the events that determine the current flow through the device as the injection of carriers from contact, the capture to the wells, thermionic emission from the wells and photoexcitation from the wells. These events are illustrated in Figure 11.

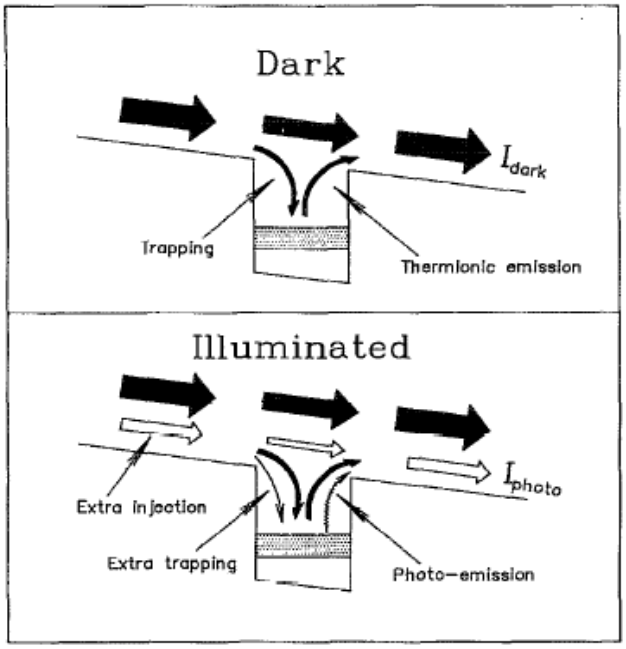

Figure 11: The events that affect the current flow through one period of a QWIP device [21]

According to this model, the responsivity arises from the extra current injected to compensate for the carriers that has been excited from the wells. Therefore, the capture probability of the electrons to the quantum wells must take part in the expression of the responsivity together with the absorption quantum efficiency. The effect of the capture probability is included in the photoconductive gain, which is found as:

$$g = \frac{(1-p)}{Np} \tag{14}$$

where p is the capture probability of an electron to a well and N is the number of periods. For the conventional photoconductors, the gain is determined as L_d/L. By this expression it is difficult to explain gain values larger than one if the contact regions are assumed to absorb the electrons. Gain values larger than one in QWIP structures imply that because of low capture probability, higher number of electrons must be injected from the contact

to balance the electrons that are excited from the wells by the photons and leave the structure.

Assuming a device structure which is uniform over the length, the absorption quantum efficiency will be proportional to the number of periods while the gain will be proportional to N^{-1}. Therefore the responsivity of the structures is not expected to change with N if all the other parameters are kept constant. This was experimentally verified by Steele et.al. [21]

Another issue about the gain of the detector is the deviation of noise gain (g_{noise}) from photoconductive gain under high bias voltages. Rehm et.al. have investigated this relationship [10] and they have found $g_{noise}=Mg$ where M is the avalanche multiplication factor. In their experimental work on 20 period structure having $In_{0.3}Ga_{0.7}As/GaAs$ quantum wells and 8.9 μm cutoff wavelength, they have observed that photoconductive and noise gains are equal until an electric field strength of~22 kV/cm.

QDIP devices are expected to produce larger photoconductive gains because of the phonon bottleneck effect. This effect is the lengthening of the carrier lifetime due to the suppression of phonon scattering process between largely spaced energy levels. This suppression originates from the need for multiple phonon processes in scattering events to conserve both momentum and energy [23].

3.2 Material Systems Used For Fabrication of QWIP and QDIP

QWIP or QDIP structures can be manufactured using different materials within III-V semiconductor family. The need for lattice matched substrates to the device structures, determine two different compounds. These can be named as the GaAs based and InP

based families. GaAs and InP substrates are the ones that are most widely used in III-V semiconductor technology. Therefore, the maturity of the growth and processing technology of these semiconductors is compatible with the promises of QWIP and QDIP devices.

QWIP detectors are usually fabricated using $Al_xGa_{1-x}As/GaAs$ material system. This system permits the fabrication of QWIPs operating in LWIR and MWIR bands. However, for operation of $Al_xGa_{1-x}As/GaAs$ in the MWIR band, using aluminum contents higher than 40% is needed. For less aluminum content, the energy barriers become too shallow for formation of intersubband energy gap corresponding to MWIR photons. At these high levels of aluminum mole fraction, the barrier material becomes an indirect bandgap semiconductor resulting in a reduction in the activation energy for ground state electrons. As a result of this reduction, higher dark current is observed [24]. To overcome this shortcoming, indium is introduced into the wells. If low indium content is used in the wells, $In_yGa_{1-y}As$ material can be utilized even though it creates strain. Since $In_yGa_{1-y}As$ material has a narrower bandgap compared to GaAs, less aluminum content can be used in the barriers. As a result, $Al_xGa_{1-x}As/GaAs/\ In_yGa_{1-y}As$ material system can cover both LWIR and MWIR bands.

The second important material system for fabrication of the QWIPs is the InP based material system. In this system, $In_{0.53}Ga_{0.47}As$ and $In_{0.52}Al_{0.48}As$ materials can be grown lattice matched to InP substrates. Furthermore, InGaAsP which is the alloy of $In_{0.53}Ga_{0.47}As$ with InP and InGaAlAs which is the alloy of $In_{0.53}Ga_{0.47}As$ and $In_{0.52}Al_{0.48}As$ can be used with various compositions all lattice matched to InP. $In_{0.52}Al_{0.48}As/\ In_{0.53}Ga_{0.47}As$ QWIP devices using $In_{0.52}Al_{0.48}As$ as the barrier material has detection spectra in MWIR region, while QWIPs with InP barriers using $In_{0.53}Ga_{0.47}As$, InGaAsP or InGaAlAs quantum wells with LWIR detection spectra have been demonstrated [25]. LWIR QWIP devices based on InP exhibit higher responsivity

with respect to the GaAs devices thanks to their higher photoconductive gain. The cause of the high gain is the lower capture probability of electrons into the quantum wells which is due to the higher spacing between Γ and L valleys in these materials [26]. InP based QWIP technology poses the advantage of production of completely lattice matched LWIR, MWIR and multi spectral structures.

QDIP devices, unlike the QWIPs, have a need for a material with large lattice mismatch to form the quantum dots using self assembly. In GaAs based QDIPs, InAs or $In_yGa_{1-y}As$ quantum dots are used along with GaAs or $Al_xGa_{1-x}As$ barriers. In the DWELL devices, GaAs or $In_zGa_{1-z}As$ material can be used as the quantum well [13,15]. These devices have response spectra lying in LWIR or MWIR band. InP based QDIP devices has also been demonstrated [27-29]. These utilize InAs quantum dots with InP or $In_{0.52}Al_{0.48}As$ barriers and $In_zGa_{1-z}As$ quantum well material for wells of DWELL structure. InP devices can also be tuned to have response in either MWIR or LWIR band.

3.3 Fabrication of QWIP FPAs

QWIP detector fabrication starts with the epitaxial growth of the designed structures using either Molecular Beam Epitaxy (MBE) or Metal Organic Chemical Vapor Deposition (MOCVD). After this step, the detectors are fabricated into arrays. Successfully fabricated arrays are flip chip bonded to the readout integrated circuit (ROIC). After bonding is complete substrate is removed and the detectors are packaged into closed cycle integrated detector dewar cooler asemblies (IDDCAs)

During this thesis work MBE was practiced as the epitaxial growth technique. Usually the machine includes one growth chamber, one preparation/transfer chamber and a

loading chamber (load lock). In some systems, chambers including metrology equipment for in situ analysis are used.

The growth chamber includes pumping system and liquid nitrogen cooled shrouds for maintaining the Ultra High Vacuum (UHV) conditions. The system includes resistively heated effusion cells for the evaporation of the source materials. Each effusion cell has one shutter in front in order to obstruct the beam when not needed. The sample is mounted on a rotating, heated sample manipulator. There is also a main shutter used just in front of the sample to block all beams directed to the sample at once. The UHV environment gives the user possibility to integrate many in situ analysis equipments. The most commonly used analysis equipments are reflection high energy electron diffraction (RHEED) system which gives information about the crystal structure and surface morphology , a pyrometer which is used for monitoring the temperature on the front side of the substrate and a residual gas analyzer (RGA) which is a mass spectrometer monitoring the gas species inside the growth chamber. RGA is used for checking if there are any impurities in the chamber and determining the type of them. A schematic illustration of MBE growth chamber is given in Figure 12 (a). The preparation and transfer chamber is used for cleaning the substrates by heating prior to the growth and it is also used as a storage space for cleaned substrates. Also it constitutes a buffer between the loading chamber which is frequently vented to air and the growth chamber in order to improve cleanliness of the growth chamber. A photograph of the METU Epineat MBE system is sown in Figure 12(b)

a)

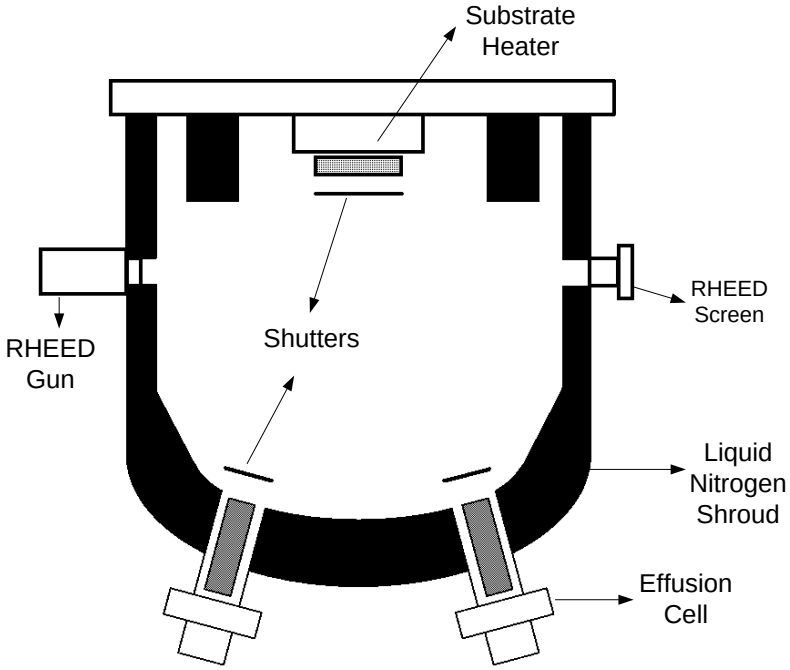

b)

Figure 12: Illustration of an MBE growth chamber (a) and the photograph of the METU Epineat MBE system (b).

During the MBE growth, the source materials and dopant materials reside in the effusion cells whose temperatures are controlled very precisely. Before the growth the beam equivalent pressure (BEP), in other words the flux, of each material is measured using an ionization gauge moved just under the sample manipulator. Once the temperatures of the cells are constant, this flux is expected not to change while growth is being done. The rate of the material growth is calibrated using the flux of the corresponding cells.

Under the substrate temperatures commonly used in growth of III-V compounds, group V species can not deposit on the surface without bonding with the group III species. Therefore the growth rate is dependant mainly on the group III element flux once the group V element flux is sufficient for growth. This feature allows the calibration to be done by using only group III flux values. When growing ternary compounds such as $Al_xGa_{1-x}As$, the mole fraction of Al inside the layer is determined by ratio of the growth rates of the two alloying materials AlAs and GaAs. As a result, once the growth rates are known, the composition of the material is also fixed and to change the composition to another value, simply the flux of the materials are adjusted accordingly.

For the doping of the structures, the dopant cells' shutters are also opened during the growth. However since dopant atom flux is very low with respect to the source atoms' flux, there is no measure of this value without growing wafers for calibration. Once wafers are grown, the amount of dopant in the layer can be found using various techniques such as Hall effect measurements or C-V measurements.

After the calibration of the cell temperatures has been done the wafer is transferred on the manipulator and heated under group V flux only. This flux maintains the quality of surface by preventing the desorption of the relatively volatile group V species. Once a certain temperature is reached, the protective oxide layer on the substrate surface is

desorbed, indicated by change in the pattern seen on the RHEED screen. The growth starts by opening the shutters of designated group III elements and dopants.

The grown layers are subjected to FPA production steps afterwards. The multi color FPAs are produced by two different approaches. First approach which is used for voltage switchable FPAs is the same as the method used in single color FPAs and needs only one indium bump per pixel . In another approach used with special ROICs designed for dual color FPAs, each pixel has three indium bumps per pixel. In the three bump approach, detectors corresponding to two different colors are working separately at the same time. This calls for one contact for each color and a common contact.

The steps of production are summarized in Figure 13. The single bump approach starts with etching of the diffraction gratings. Afterwards, mesa etch is done in order to isolate the pixels from each other. Then ohmic contact metals are deposited and annealed. Then reflector layers are deposited on top of the mesa structures, in order to have a reflecting layer behind the diffraction gratings. Afterwards, the passivation is deposited and the contact points are etched through the passivation down to the contact metal. Later Under Bump Metallization (UBM) layers are deposited. These layers provide a surface where indium bumps can stick easily and also prevent the diffusion of indium into the detector material when heated during flip-chip bonding (FCB). Indium bumps are electro-plated on top of UBM layers afterwards. When these steps are complete, the chip is diced and flip chip bonded to ROIC. To ensure mechanical strength an underfill epoxy is injected between the ROIC and detector after FCB. Since there is a mismatch of thermal expansion coefficient between the silicon ROIC and detector made of III-V compound, the cooling to cryogenic temperatures can cause cracks in the FPA. Therefore FPA's go through substrate removal process after underfill epoxy is cured. The substrate is thinned to leave the active layers and a few micrometers of bulk material. These in total have thickness of approximately ten micrometers and at this thickness the layer can withstand

the stress caused by thermal mismatch. The process is finalized by deposition of anti-reflection coating

The processing of the three-bump pixels exhibits certain differences. After the diffraction gratings are etched the mesa etch is done at three steps in this approach. In three-bump detectors there is a need for separately obtaining contact from top bottom and middle contact layers for each pixel. Also since the bottom contact will not be the common contact, each pixel must be etched once more down to semi insulating substrate for isolation. This results in three etch steps one to reach middle contact, one to reach bottom contact and one for isolation. Also one additional metal layer is needed to carry the contacts from the etched regions to the top of the pixel where indium bumps will be placed. An illustration of a pixel fabricated by this method is given in Figure 14.

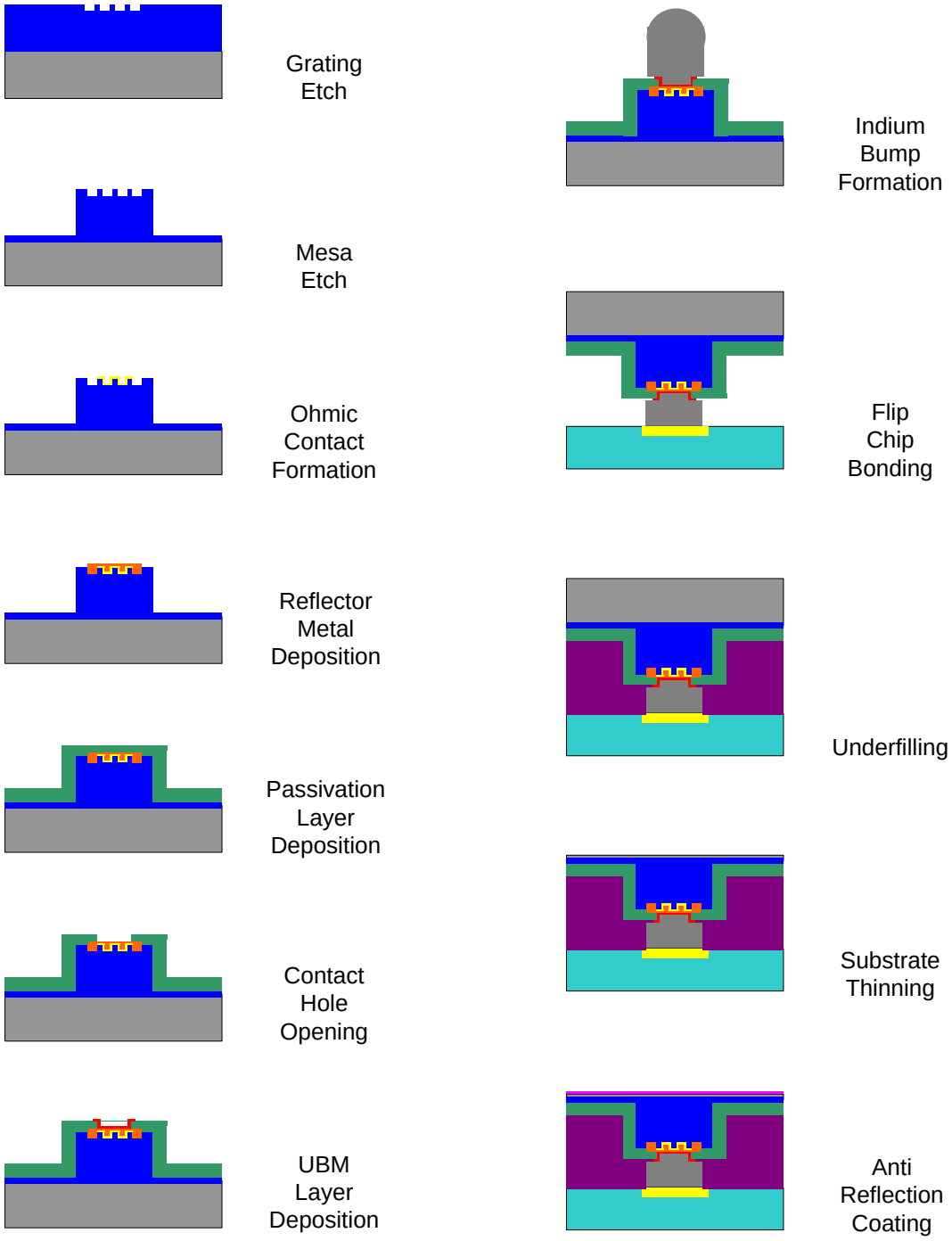

Figure 13: Summary of QWIP FPA fabrication steps.

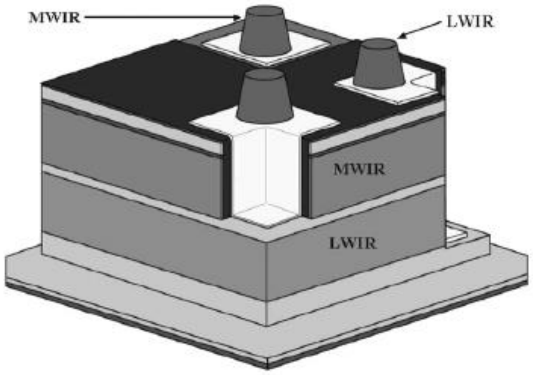

Figure 14: An FPA pixel fabricated by three bump approach [30]

3.4 State of the Art in QWIPs

After more than a decade from the demonstration of first QWIP camera, the QWIP device technology has advanced so that 640×512 arrays are available commercially. Currently research and development work is concentrated on larger format arrays and multi spectral devices. Besides this research, work is also conducted to increase the sensitivity of the structures.

Gunapala et. al. has demonstrated 1024×1024 QWIP FPAs one working in MWIR and the other in LWIR region [30]. These FPAs utilize standard $Al_xGa_{1-x}As/GaAs$ and $Al_xGa_{1-x}As/GaAs/In_yGa_{1-y}As$ material system. The only difference compared to the conventional QWIPs is that, the quantum wells in the MWIR detector are formed by coupling two wells by separating them with a thin barrier. This increases the broadness of the spectrum. These devices have 19.5μm pitch and 17.5 μm actual pixel sizes. MWIR QWIP has 5.1 μm cutoff wavelength with $\Delta\lambda/\lambda$ of 15%. The quantum efficiency was found as 19%. It was found to have $4x10^{11}$ cm√Hz/W detectivity at 90 K operating temperature and f/2.5 optics. MWIR FPA yielded 23mK NETD at 90 K operating

temperature, 60 ms integration time and f/2.5 optics. The operability of this FPA was larger than 99.95%. The LWIR device yielded NETD of 16 mK at 72 K operating temperature using f/2.5 optics and 29 ms integration time. The operability was determined as 99.98% at these conditions.

In the area of multi spectral QWIPs, most of the work is done on the LWIR/MWIR dual band detectors. The work on the LWIR/LWIR and MWIR/MWIR dual color detectors is very limited. So far the only reported MWIR/MWIR QWIP FPA is the one reported by Sundaram et.al. in 2001 [31]. This 256×256 device was fabricated by three contact approach and the pixel pitch is 50 μm. The two colors have peak responsivity wavelengths at 4μm and 4.7 μm respectively. These two colors yielded NETDs of 41mK and 32mK respectively at 85-90K operating temperature, using 8-10ms integration time and f/3 optics.

LWIR/LWIR multicolor FPAs were also reported by Sundaram et.al in the same publication. These 256×256 FPAs were again fabricated by three contact approach but they have 40 μm pitch. The peak responsivity is attained at ~8 μm and ~11 μm wavelengths for two colors. The NETDs were 22mK and 15mK for these colors respectively. NETD measurement was done at 40K detector temperature and 100Hz frame rate with f/3 optics. At 100 Hz frame rate the maximum integration time can be 10ms.

In 2007 Gunapala et.al demonstrated a 320×256 LWIR/MWIR dual band QWIP imager [30]. This FPA has 40 μm pixel pitch. The responsivites of LWIR and MWIR bands have peaks at ~8.5 μm and ~4.8 μm respectively. The NETD values found using f/2 optics at 65K detector temperature are 28mK and 38 mK respectively. Operability is reported to be greater than 95%.

Schneider et.al. have reported a LWIR/MWIR dual band QWIP FPA based on three contact approach in 2004 [32]. This FPA has 384×288 resolution and the pixel pitch is 40 μm. The peak responsivity wavelengths in LWIR and MWIR bands are ~4.9 μm and ~8.2 μm, respectively. The measured NETDs with 7.6 ms integration time and f/2 optics are 17 mK and 43 mK in MWIR and LWIR bands, respectively.

So far the only voltage tunable FPA is the DWELL QDIP device reported by Varley et.al.[33] This MWIR/LWIR 320×256 FPA demonstrates a poor switching behavior and the NETD values measured are 55mK and 70mK for MWIR and LWIR bands, respectively.

The part of this thesis work on the lattice matched InP based MWIR QWIP FPA will be presented in the next chapter.

CHAPTER 4

LATTICE MATCHED MWIR QWIPS ON InP SUBSTRATE

MWIR QWIPs based on the $Al_xGa_{1-x}As$/ $In_yGa_{1-y}As$ system has certain disadvantages due to the strain included in the growth of $In_yGa_{1-y}As$ material. The overall thickness of the structure is limited by the total strain induced. Thus the thickness of the $In_yGa_{1-y}As$ well layers, and therefore the total number of periods has an upper bound [34] limiting the possibility of increasing the number of periods to have higher absorption quantum efficiency without using special relaxation layers in growth [35].

In order to overcome these limitations the $In_{0.52}Al_{0.48}As$/ $In_{0.53}Ga_{0.47}As$ material system which is lattice matched to InP can be used. In this material system $In_{0.53}Ga_{0.47}As$ having lower bandgap is used as the quantum well whereas $In_{0.52}Al_{0.48}As$ constitutes the barriers. This material system is also advantageous in coupling MWIR QWIPs with the $In_{0.53}Ga_{0.47}As$/InP or InGaAsP/InP LWIR QWIPs [1]. By this way, the InP based QWIP detectors can cover both MWIR and LWIR windows to constitute an important alternative to the GaAs based QWIPs.

However the research done on the $In_{0.52}Al_{0.48}As$/ $In_{0.53}Ga_{0.47}As$ MWIR QWIPs is not as extensive as the strained counterpart. Levine et.al. [36] have first investigated this structure using 50 Å wells and 100 Å barriers obtaining 4.4 μm peak absorption wavelength and 7% $\Delta\lambda/\lambda$ value. In the work of Hasnain [37], using 30 Å wells and 300 Å barriers, absorption peak at 4.44 μm (279meV) was achieved with FWHM of 93 meV.

The peak responsivity (25 mA/W) of this structure was at 4 μm. Responsivity spectrum had $\Delta\lambda/\lambda$ of 17.5%.

The first large format FPA based on $In_{0.52}Al_{0.48}As$/ $In_{0.53}Ga_{0.47}As$ material system was demonstrated by our group [38]. This sensor which utilizes 26 Å thick wells, had peak responsivity at 4.2 μm and higher cutoff wavelength at 4.6 μm.

In the course of this thesis, more work has been done on the InP based MWIR QWIPs to grow the structures in house and improve the performance by broadening the spectrum.

4.1 MBE Growth of the Epilayer Structure

QWIP devices are fabricated using III-V group semiconductors as discussed in section 3.3. The structures are formed by sandwiching a very thin layer of the quantum well material between the relatively thick barriers. The quantum well thickness is between 10-100Å while the barriers are usually 300-600 Å thick. Growth of these structures in a precise fashion requires very fine tuning of the growth parameters.

As described in section 3.3, effusion cell temperatures are adjusted to control the composition and the growth rate of the materials. The dopings of the samples are adjusted with the temperature of the dopant effusion cell. In addition to these, adjustment of the wafer temperature during the growth is needed to obtain good layers.

Before each growth, the BEP of the source materials are measured and calibrated by changing the cell temperatures. The temperatures of the effusion cells may be affected from the opening and closing of the cell shutters since a considerable amount of infrared radiation is reflected back to the cell when closed. When the cell shutter is opened, this

radiation is lost and temperature of the cell may have a transient. In the case of the growth of the quantum wells, this temperature transient changes the flux of the source temporarily and causes the composition of the quantum well material to be different than the composition calculated using steady state values. To overcome this difficulty, special ramps in cell temperature are applied before or during shutter opening. These are also tested by using a similar recipe to the quantum well growth. Similar ramps are also applied during the start of growth of $In_{0.53}Ga_{0.47}As$ contact layers also. The optimization work for InP based MWIR QWIPs includes finding the ideal flux ratios for the growth of lattice matched well and barriers, adjustment of the substrate temperature and adjustment of doping in the $In_{0.53}Ga_{0.47}As$ material.

4.1.1 Optimization of $In_xAl_{1-x}As$ and $In_yGa_{1-y}As$ Compositions

Calibration growths have been made in order to optimize the $In_xAl_{1-x}As$ mole fraction so that the $In_xAl_{1-x}As$ material is lattice matched to the InP. In these trials while the indium flux is held constant, the aluminum flux has been changed. The indium flux is intended to stay constant throughout the growth of $In_xAl_{1-x}As/In_yGa_{1-y}As$ multi quantum well structures since abrupt changes in the flux needs abrupt changes in the temperature of the effusion cell which may result in instability of the temperature and flux.

After the growth of the wafer, X-ray diffraction (XRD) rocking curve measurements have been performed to find the mole fraction of Indium and Aluminum in the structure. The result of these measurements for an optimized growth is given in Figure 15. In this figure it is clearly seen that sample numbered InP34, which was grown at the optimized conditions, has $In_{0.52}Al_{0.48}As$ composition which is lattice matched to InP since no secondary peaks can be resolved. The full width at half maximum of the obtained rocking curve is 0.0156 seconds.

The mole fraction of $In_yGa_{1-y}As$ layers were characterized directly from the XRD measurements made on the grown QWIP structures. Values of indium mole fraction 0.53 ± 0.01 were obtained usually in the growths which are very close to lattice matched composition of 0.53.

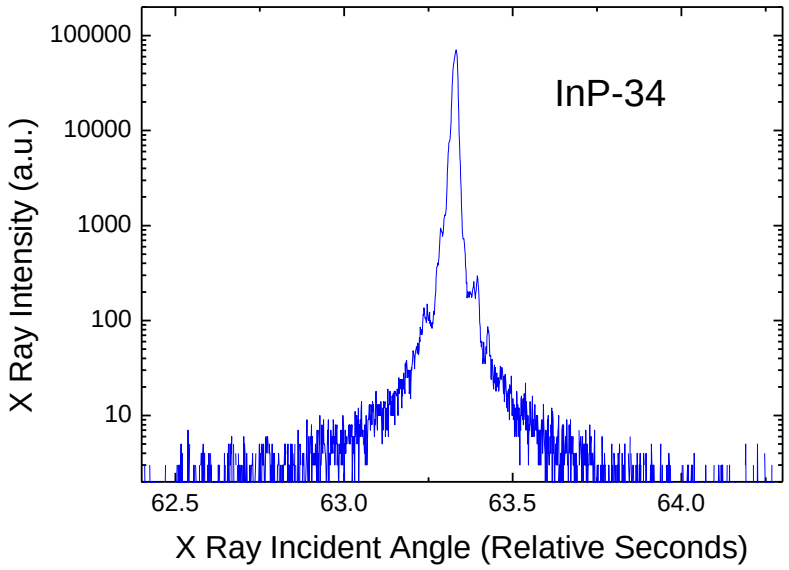

Figure 15: The X-ray diffraction rocking curve for grown $In_xAl_{1-x}As$ sample with the optimized growth conditions.

4.1.2 Optimization of Substrate Temperature

For the growth of $In_{0.53}Ga_{0.47}As$ layers on InP, first the growth was started at around 480°C substrate temperature with InP buffer layer. When the growth of $In_{0.53}Ga_{0.47}As$ started, an increase in the substrate temperature was recorded with the pyrometer

mounted. The reason for increase in temperature during the growth of relatively narrow bandgap semiconductors on GaAs or InP was first discovered by Shanabrook et. al. [39]. In their work they have concluded that the narrow bandgap semiconductors absorb more radiation from the filaments of the substrate heater, increasing the temperature as the grown layer becomes thicker. For reducing the temperature increase, different techniques were used, which decrease the heater temperature by providing substrate temperature feedback to the system [40, 41]. The reason for the poor quality of layers grown at high temperatures is the decrease in the growth rate of InAs in the alloy $In_xGa_{1-x}As$ [42] resulting in an indium composition far from lattice matched value. .

To overcome this issue a special ramp-down for the temperature of the heater was used and the substrate temperature was adjusted to stay within ±5°C of the starting temperature. The ramp down is determined by the rate of increase in the temperature of the samples observed when the heater temperature was left untouched. The substrate temperature was seen to be stable after some point indicating that the heat absorbed was approximately equal to the heat radiated by the substrate. When the growth of $In_yAl_{1-y}As$ barrier layers started after the contacts, a rapid decrease of around 10°C in substrate temperature was observed which was attributed to the different emissivity of $In_yAl_{1-y}As$ layer.

4.1.3 Optimization of Doping

For the n-type doping of the layers, Si was used as the dopant. The calibration of the doping in structures was done by growing calibration layers and then determining the concentration of doping with Hall Effect measurements. The measurements were done on the InGaAs samples grown on InP substrates. After the measurement of the calibration samples, the trend line for the doping was set and the further growth was

done by choosing the Si cell temperature corresponding to the desired dopant concentration.

4.2 FPA Performance

The InP based MWIR QWIP structure was grown in our laboratory using Riber Epineat MBE system. The structure includes 30 periods with one period consisting of a 23Å $In_{0.53}Ga_{0.47}As$ quantum well and a 300 Å $In_{0.52}Al_{0.48}As$ barrier. The quantum wells are n-type doped with Si to a concentration of 4×10^{18} cm^{-3} and the barriers are undoped. The multi quantum well stack is sandwiched between $In_{0.53}Ga_{0.47}As$ top and bottom contact layers which are doped with Si with the concentration of 1×10^{18} cm^{-3}.

A 640×512 FPA was fabricated, with this wafer using the techniques summarized in section 3.3. During the fabrication of the FPA, wet etching was used for forming the mesa structures. Due to the unavailability of nanoscale lithography tools, a diffraction grating structure with a period realizable with optical lithography was utilized [43]. The fabricated FPA is bonded to an Indigo ISC9803 ROIC.

After the bonding and substrate removal was completed, the characterization was done both on the FPA itself and on the test detectors fabricated with the FPA. These test detectors were fabricated on the same die with the FPA, going through the same fabrication steps with the FPA itself. Therefore the characteristics of the test detectors are identical to the FPA pixels. This feature of the test detectors is important since certain features of the detectors such as light coupling (therefore quantum efficiency) is reported to change with the varying pixel size [44]. The test pixels were flip chip bonded to fanout substrates for characterization with backside illumination. In the fanout substrates, the contacts were taken from groups of 25 pixels parallel connected in 5 pixel×5 pixel arrays. Furthermore several groups were connected in shunt with wire

bonds outside the fanout substrate to obtain signal and noise levels above the noise levels of instruments. The test detectors were mounted in a liquid nitrogen cooled dewar with f/1.5 aperture and an anti-reflection coated window transparent in the 3-12 μm range. After the detectors were cooled to 80 K, the dewar was placed in an Fourier Transform Infrared (FTIR) Spectrometer and connected to a transimpedance preamplifier.

The spectrum of the infrared light source of the FTIR Spectrometer was first measured with a pyroelectric reference detector having wavelength independent response. Later, the response obtained from the QWIP structure under test was divided with the reference data by the FTIR software to obtain the true responsivity spectrum of the detector. By this way, the effects of the spectral distribution of photons emitted from the IR source and the absorption of air is cancelled. The test setup is drawn in Figure 16. This setup does not facilitate any means for measuring the optical power falling on the detector. As a result, the measured spectrum levels have arbitrary units. Therefore, the responsivity spectra are normalized to have peak values of one after the data is obtained.

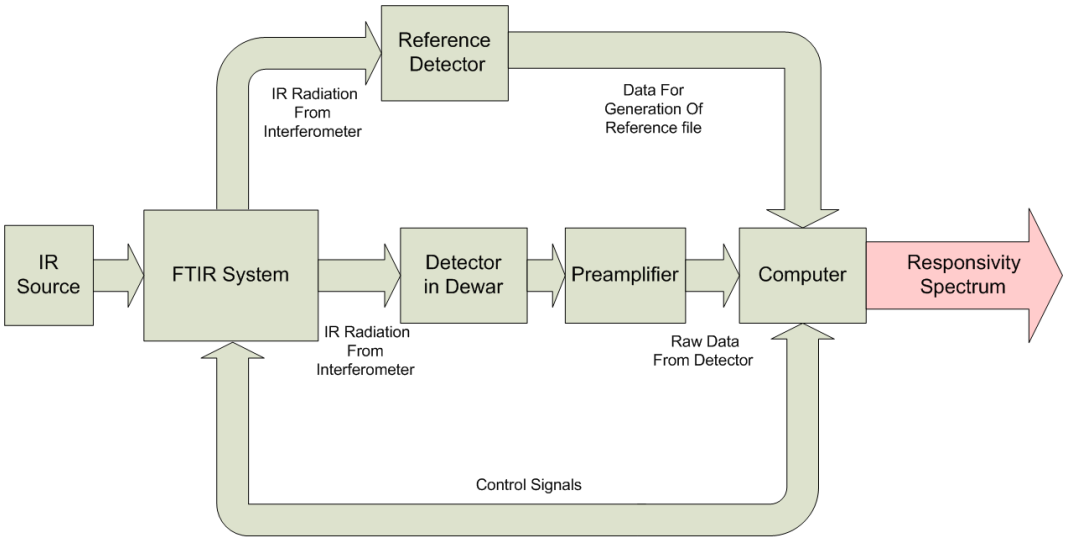

Figure 16: The setup used for obtaining the responsivity spectrum of a detector.

In Figure 17, the normalized responsivity spectra of the sample grown in our laboratory can be seen alongside with two other samples having 30 Å and 26 Å quantum well widths which were grown at IQE Inc. and processed in our laboratory

The QWIP structure with 23 Å quantum well width has responsivity peak at 4.18 μm, with higher and lower cutoff wavelengths at 4.9 μm and 3.5 μm respectively. The $\Delta\lambda/\lambda$ of the detector is 32%. The lower cutoff wavelength and peak detection wavelengths of the structures do not change with the quantum well width significantly. However, the higher cutoff is shifted from 4.9 μm to 4.15 μm resulting in a considerably narrower spectrum. Detection at the wavelengths as close as possible to 5 μm is important, since the photon flux of near room temperature objects that are is higher at these wavelengths with respect to the wavelengths closer to 4 μm. Therefore the structure having 23 Å quantum wells poses an advantage in the performance.

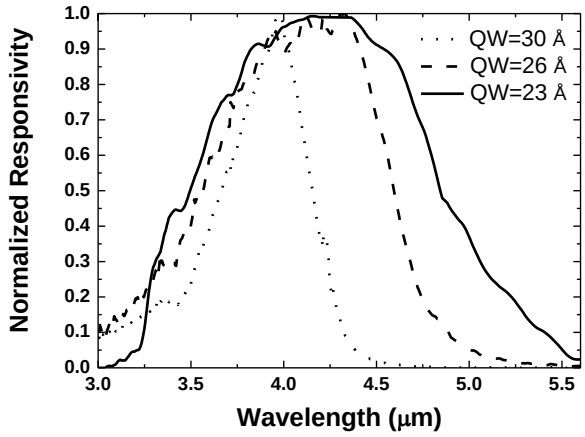

Figure 17: Normalized responsivity spectra of InP based MWIR QWIP structures with different quantum well widths.

The photocurrent of the FPA pixels was measured on the test detectors as a function of bias, while they were exposed to radiation from 300K background with an f/1.5 optical aperture at 80K operating temperature. The loss of light due to the reflection from the substrate was taken into account in the photocurrent measurement. Later, the dark current of the pixels was also measured at various temperature levels. The measurement results can be seen in Figure 18. When we compare the dark current values with the photocurrent, we observe that the FPA is BLIP at 115K temperature, until a bias of 2.75 V.

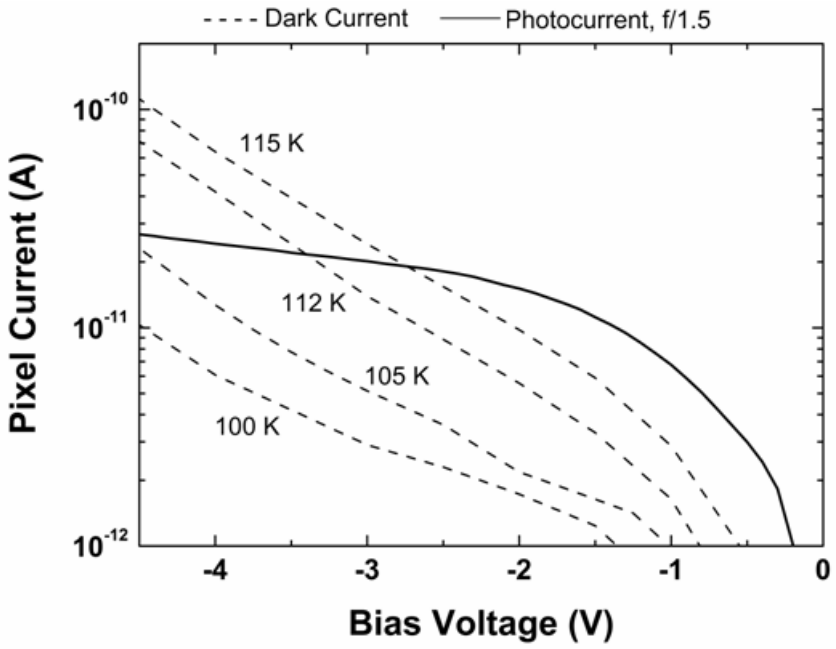

Figure 18: The dark current values for various temperatures and the photocurrent (with f/1.5 aperture) of one FPA pixel as a function of bias voltage.

Using the dark currents obtained at different temperatures, the activation energy of the quantum wells was obtained using the formula [17]:

$$\frac{I_{dark}}{T} \propto e^{\frac{-(E_C - E_F)}{kT}} \tag{15}$$

where E_C denotes the energy gap between the top of the barrier and the ground state of the quantum well, E_F is the Fermi level of the electrons inside the quantum well. E_C- E_F thus is equal to the activation energy for the electrons E_A. The calculated activation energy values can be seen in Figure 19. Activation energy was found to decrease with the increasing bias due to barrier lowering effects [45].

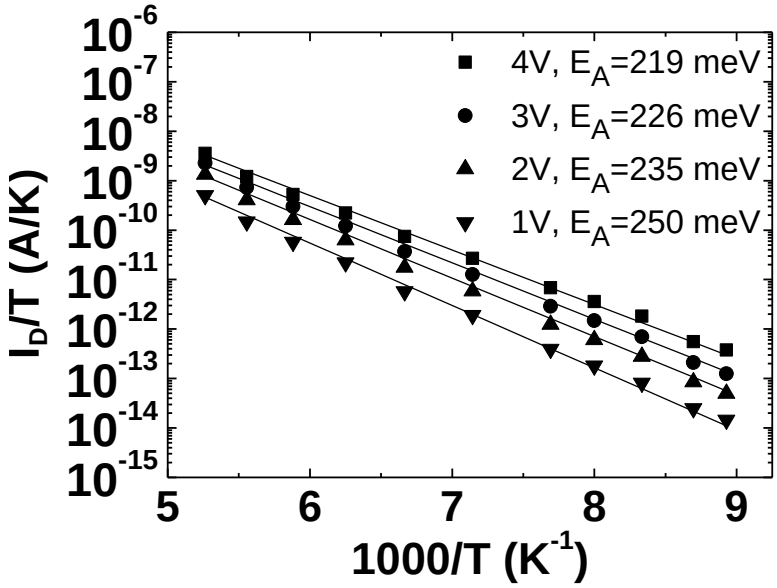

Figure 19: The calculated activation energy values as a function of bias.

After the above measurements, the responsivity and detectivity of the test detectors was measured. For these measurements a blackbody source with a chopper, a lock-in amplifier, a transimpedance preamplifier and a computer with specialized software were used. The measurement setup is given in Figure 20. For the responsivity measurement the blackbody source was adjusted to 500°C and the chopper in front of the blackbody source was adjusted for 5 Hz speed. The detector was placed in front of the blackbody source and connected to the preamplifier. The output signal of the preamplifier was fed into the lock-in amplifier measuring the signal level at 5 Hz. The computer then divides the signal by the optical power falling on the detector, which is calculated by the software once the distance of the detector to blackbody, detector area, window transmission and the diameter of blackbody aperture are known. By this way, the voltage responsivity of detector-preamplifier combination is found. To find the current responsivity of the detector, the measured voltage responsivity is divided by the transimpedance gain of the preamplifier.

In order to calculate the detectivity, the noise of the detector was measured. For measuring the noise, the blackbody chopper was stopped and the cavity of the blackbody was obstructed to leave the detector looking at background of the room. In this condition, the noise level at 5 Hz was measured by the lock-in amplifier. Since the lock-in amplifier does the measurement in a narrow bandwidth, this measured noise level is the noise spectral density at 5 Hz. Since the noise spectral density, area of the detector and the responsivity is known the detectivity is calculated by the software using the formula 9.

However, the measured responsivity and detectivity values are blackbody responsivity and blackbody detectivity values. This means that the detector is assumed to be a black box by the system and the power falling on the detector is calculated as the whole power emitted by the blackbody source. To take into account the shape of the responsivity spectrum of the detector, peak factor is calculated. For calculation of the peak factor, the integrated blackbody spectrum (Planck distribution) is divided by the integration of the

blackbody spectrum multiplied by normalized detector responsivity. This is equivalent to interchanging the spectral response of the detector with its actual spectrum, instead of wavelength independent spectrum assumed by the software. When the blackbody responsivity and detectivity values are multiplied with the peak factor obtained, the responsivity and detectivity at their peak points in the spectrum is found. This procedure is summarized in Figure 21

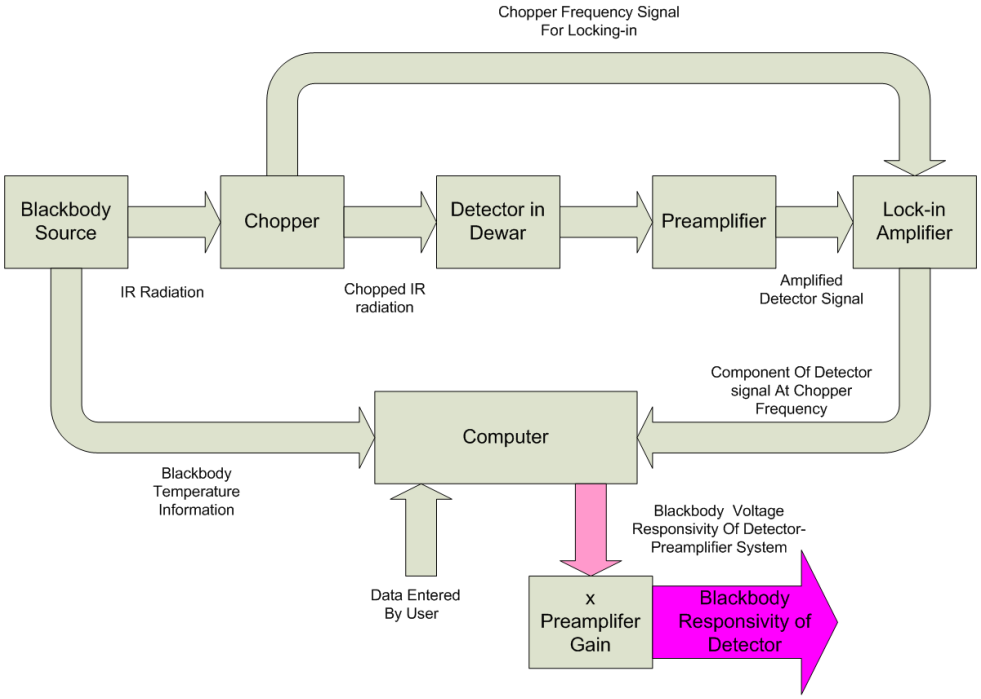

Figure 20: The setup used for obtaining the responsivity of the detectors.

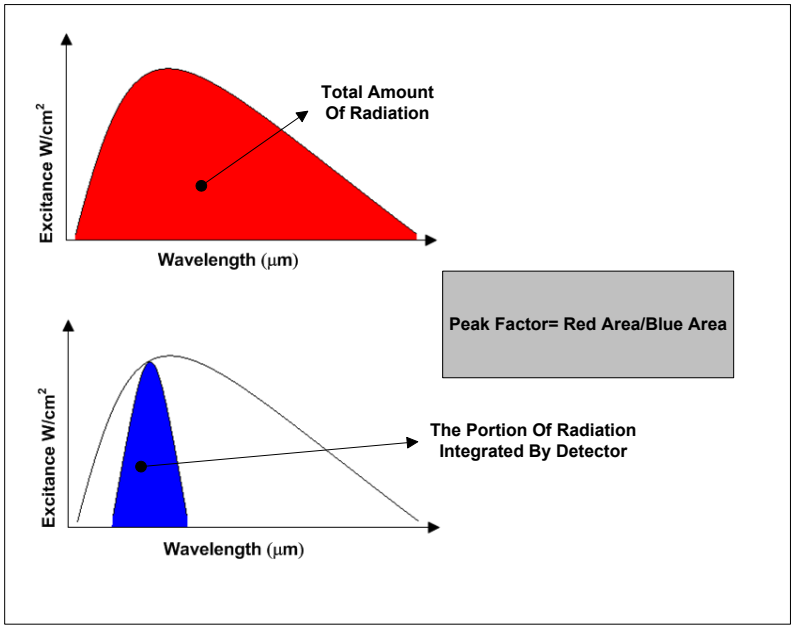

Figure 21: The summary of peak factor calculation procedure.

The dependence of the peak detectivity and peak responsivity on the reverse bias of the detector, measured at 80 K detector temperature with f/1.5 aperture can be seen in Figure 22. The responsivity tends to saturate at higher bias values, unlike the LWIR QWIPs grown on InP substrates utilizing InP barriers [1]. This is thought to be due to the higher spacing between Γ and L valleys of InP with respect to $In_{0.52}Al_{0.48}As$ [46].

The gain of the structure was found using the noise and the total current measured at 80K by the help of equation 6. Using the obtained gain value, the detectivity of the pixels was determined at different temperatures for 2.5 V reverse bias, 300 K background and f/1.5 aperture. For this calculation, the dark currents measured at different detector temperatures were summed with the photocurrent to find the total current at these temperatures. The noise current was calculated at different temperatures using the value of total current, and the gain values. Using the noise current and responsivity, detectivity

was calculated using equation 9. The resulting dependence of detectivity on the detector temperature can be seen in Figure 23.

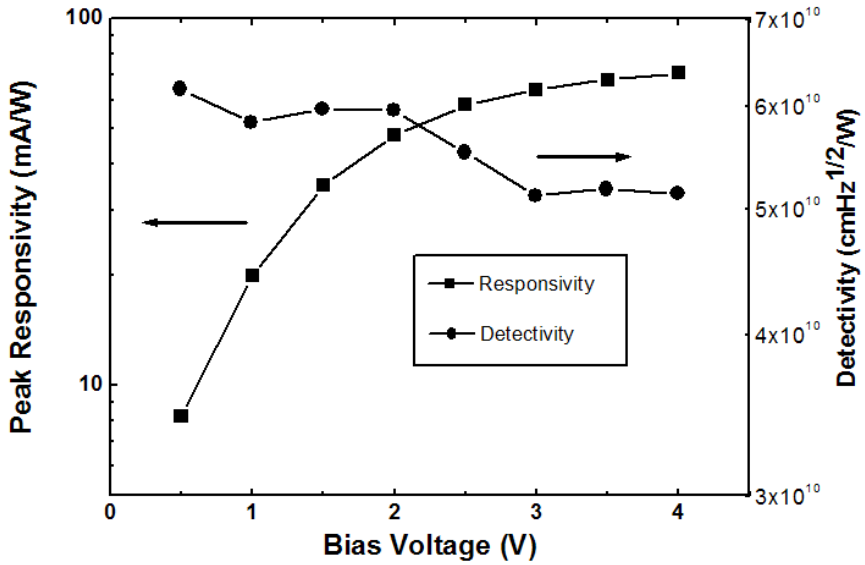

Figure 22: The peak responsivity and peak detectivity of test pixels versus the reverse bias.

NETD, non-uniformity and operability tests were performed on the FPA. During the measurements, the FPA was placed in a liquid nitrogen cooled dewar with f/1.5 aperture and anti-reflection coated window transparent in the 3-12 μm range. The output pins of the ROIC were connected to the camera electronics with 14-bit ADC resolution

Using this setup, two sets of images were obtained while the FPA was looking at a large area differential blackbody source and the reference plate of this source which was at room temperature. The obtained data sets include successive 128 frames to measure the temporal NETD of the pixels. First the data set was obtained with the reference plate and then with the blackbody source which was 12 K hotter than the reference plate. For each

pixel, the difference between the average digital level of the two data sets gives the response to 12 K temperature difference. The noise was obtained by calculating the standard deviation of the signal in time for the first data set, for each pixel. NETD was calculated by dividing the noise by response and multiplying by 12 K. The mean NETD of the FPA was calculated afterwards by averaging the NETD values of the pixels. The pixels having NETD values more than two times the average value of the NETD were regarded as "dead" pixels. The operability was calculated as the ratio of working pixels to the total pixels. The DC signal non-uniformity was found by dividing the standard deviation of the signal over the array by the average signal

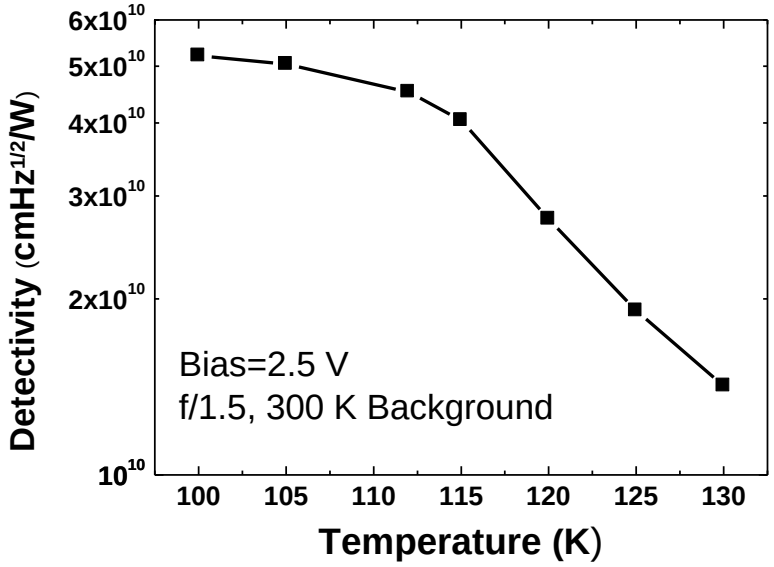

Figure 23: The detectivity of the test pixels versus FPA temperature calculated using data obtained from the measurements.

The NETD value at 3.5 V reverse bias, 80 K detector temperature and 20 ms integration time is 22 mK. The operability of the FPA is determined to be ~99%. The DC signal nonuniformity is 6.4% without any correction.

Using the detectivity values at different temperatures, the NETD at 2.5 V reverse bias was calculated with 20ms integration time and f/1.5 optics by the help of equation 13. The values obtained are given in Figure 24. These results suggest that the FPA is able to work at temperatures up to 115 K yielding reasonably low NETD. The high temperature of operation is expected to decrease the cooler power consumption, which is important for portable devices.

Figure 25 is the image of a person taken with the detector operating at 80 K temperature, with -3.5 V reverse bias and 20 ms integration time. The blood vessels on the hand are clearly visible, confirming high sensitivity.

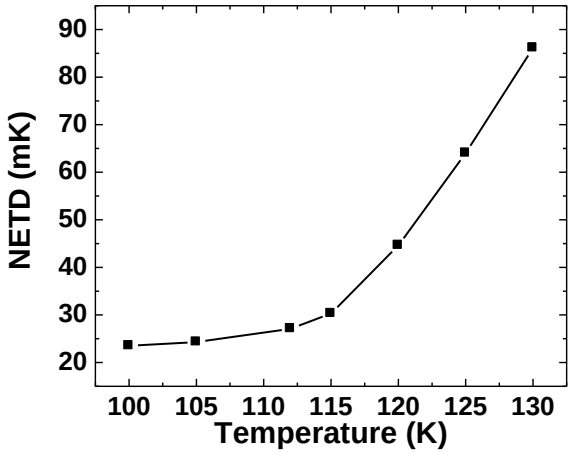

Figure 24: The NETD of the FPA versus detector temperature calculated using the detectivity data of the pixels.

Figure 25: 640×512 image of a person taken with the InP based MWIR detector operating at 80 K

4.3 Conclusion

This work demonstrates, promising results for InP based QWIPs operating in the MWIR spectral band. The lattice matched material provides the possibility of growing high number of wells which increases quantum efficiency of the structure. The NETD values obtained in our work is comparable with the values obtained in the literature with the MWIR sensors. The grating structure can be improved by printing finer features and the fill factor of the structure can be increased using reactive ion etching instead of wet etching. By assuming a two fold increase in the signal with the above mentioned improvements NETD values close to 10 mK can be achieved.

MWIR QWIP detectors having high sensitivity at high operating temperatures can be used in the systems where high resolution and low NETD values are needed along with low power consumptions. Figure 26 shows the power consumption of an IDDCA versus FPA temperature with potential detector applications in these temperature ranges. The power consumption of the assembly decreases drastically with increasing FPA temperature. InP based MWIR QWIP FPAs providing low NETD values and BLIP operation at elevated temperatures alongside with low cost provided by III-V technology can be used to fabricate high performance devices with low power consumption

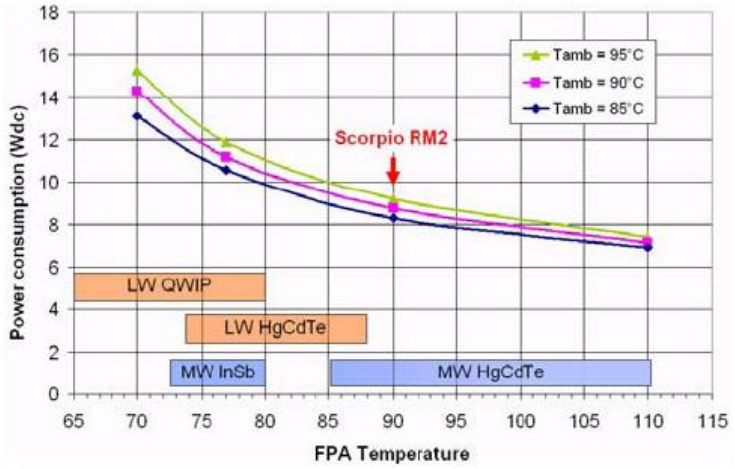

Figure 26: Power consumption of an IDDCA as a function of FPA temperature [47].

CHAPTER 5

DUAL COLOR MWIR/MWIR QWIP FPAS

The third generation infrared imaging systems are expected to deliver increased resolution, increased temperature sensitivity and multispectral imaging capability. The ability to sense the infrared radiation in two or more distinct wavelength ranges in the infrared spectrum will increase the sensor's resistance to countermeasures, background clutter and camouflage. These advantages are mainly due to possibility of eliminating the effect of emissivity of the objects to the obtained images.

While using single band detectors, the obtained signal due to the infrared radiation emitted by an object is a function of its temperature and emissivity as described in section 2.1. However, if a system with two different wavelength bands is used, with the assumption that the emissivity does not change considerably between these bands, the images from two different bands can be processed to have the resultant image dependant on the temperature only. Theoretically, if the objects are perfect greybodies, the absolute temperature can be deduced, since the ratio of the signal obtained in two wavelength bands can be calculated using Planck distribution as a function of temperature.

In addition to the general advantages of multispectral IR imaging, the MWIR/MWIR dual color detection has certain features. Sarusi has investigated the washout phenomena observed in the use of wideband MWIR FPAs during daylight conditions [48]. As it can be seen in Figure 27, the integrated number of photons detected can be equal for both background and high temperature targets due to the scattered sunlight. However, if the

MWIR spectrum is divided in two different color ranges, one can distinguish between the wavelength regions where the background radiation or target radiation is higher.

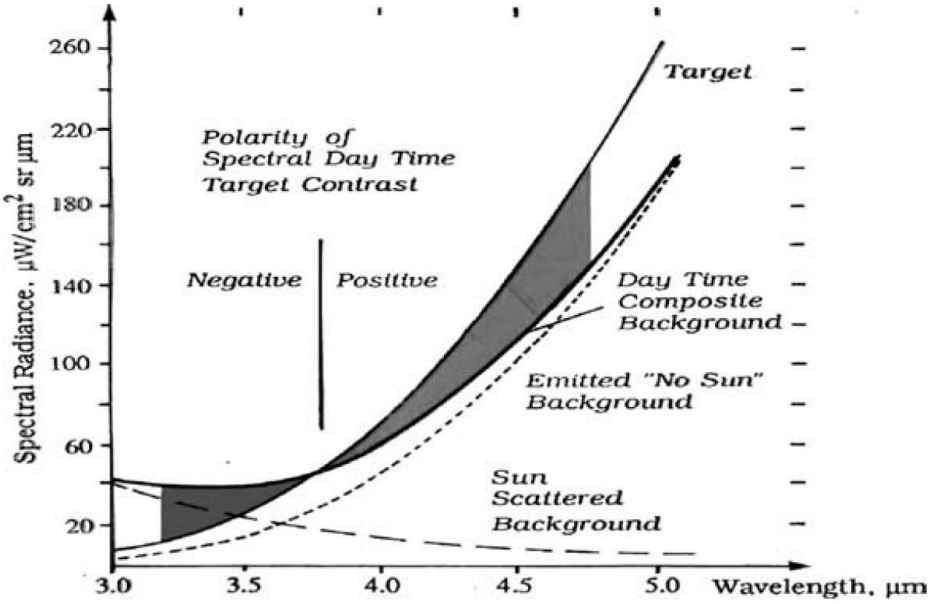

Figure 27: The comparison of spectral radiance from background and target at daytime conditions and demonstration of the washout phenomenon [48].

Furthermore, Cabanski et.al. [8] have developed a method for the determination of hot CO_2 gas using dual color MWIR/MWIR detectors. Their approach aims missile approach warning, and uses the high amounts of hot CO_2 gas released by the missiles. The hot CO_2 gas is found to emit radiation in a narrow band between ~4.4 and ~4.7 μm considerably higher than the remaining of the infrared spectrum [47]. If one of the colors (blue) is tuned to detect below 4.2 μm and the other (red) above 4.4 μm wavelengths, the ratio of the signal of red to blue is found to be very high in hot CO_2 gas compared to greybody objects and the radiation of the Sun. By this way, the false alarms caused by the Sun and the moderately hot objects which are close to detector or background clutter can be

reduced. Although it is discussed by Cabanski et.al [8] that the low frame rates achievable by QWIP detectors prevent use in the missile approach warning applications, the ability to detect hot CO_2 gas can be advantageous in land applications or civilian use .

There is less work on the MWIR/MWIR dual color detectors when compared to MWIR/LWIR detectors. This is thought to be because of the limited field of use for these detectors. Rehm et. al. have investigated MWIR/MWIR Type II superlattice detectors fabricated with the three bump approach [50]. The 384×288 FPA has two colors with cutoff wavelengths of 4μm and 5μm. The NETD values measured in these bands were 29.5 mK and 16.5 mK, respectively. During the NETD measurement, 73K detector temperature, f/2 optics and 2.8 ms integration time were used. The operability values were reported as 98% and 99% for the channels having 4μm and 5μm cutoff wavelengths, respectively.

Work on back to back diodes for voltage switchable response is also realized with HgCdTe detectors [51]. However, the work in the field of QWIP for MWIR/MWIR FPAs is limited to the three bump per pixel FPA reported by Sundaram et. al. [31] which yielded 32 mK and 41 mK NETDs in red (4.7μm) and blue (4.0 μm) bands, respectively, with f/3 optics, 8-10 ms integration time and at 85-90 K detector temperature. Although LWIR/MWIR voltage tunable QWIPs have been studied by various groups [19,52,53] there has not been any work reported on MWIR/MWIR QWIPs except the Si/SiGe structure reported by Rauter et. al. [54], which yielded detectivities on the order of 10^9 $cmHz^{1/2}/W$ for both colors at 77 K operating temperature. The aim of the detectors investigated in this thesis work is to use the low pixel outage and high resolution of single bump FPAs together with voltage switchable structures to fabricate dual color large format MWIR/MWIR QWIP arrays.

Liu et.al. has investigated the voltage tunable stacked QWIP structures in detail [55]. They have developed a model to observe that switching is dependant on the voltage drop on the individual detectors, the photocurrent generated in individual stacks and the dynamic resistances of the QWIP stacks. They have performed experiments on QWIPs having 7.5 μm and 10 μm peak responsivity wavelengths in color 1 and color 2, respectively. They have used two samples to examine the effect of the bound to bound and bound to continuum nature of the stacks to the switching characteristics. One of the samples has color 1 stack as a bound to bound QWIP and color 2 stack as a bound to continuum QWIP while the second sample has the opposite arrangement. They have discovered that there was no substantial difference in switching. They have concluded that if one stack is converted from bound to bound to bound to continuum, the voltage drop on the stack decreases as a result of decreasing resistance. However, the expected decrease in the signal resulting from the less voltage drop on the stack is compensated by increase in the responsivity of the stack. As a result no net change is observed in the overall character.

Indeed, this can be generalized to various parameters in the design of the structures. These parameters can be listed as below for each stack:

1) The detection wavelength,
2) The doping of the wells,
3) The number of periods,
4) Bound to bound or bound to continuum nature.

An increased detection wavelength or using a bound to continuum structure increases the probability of escape from the wells, due to the lowering of the barriers. As a result, the responsivity and the total current of the structure increase. Increase in well doping also

increases the current and responsivity, since more electrons will be excited from the wells.

Decreasing the number of periods increases the electric field on the structure, resulting in higher signal in lower bias ranges, because of the increase in the gain. Also saturation of photoresponse at lower biases will be observed, since the saturation occurs after a certain electric field value.

In this scheme, the parameters increasing the response of one stack all decrease the resistance of the stack resulting in less voltage drop and therefore less electric field on the stack. By this way, increase in response from one stack is hindered by the decrease in the voltage drop on this stack. This feedback mechanism of the structure parameters makes the design process complicated.

The goal of this thesis work is to have reasonable switching at the desired wavelengths and it is achieved by trying to find the optimum number and periods doping for each stack. Also the sensitivity wavelength can be a parameter as long as it stays in the desired limits. However, since the atmospheric transmission window is narrow in MWIR band and there is a low transmission region inside this band because of CO_2 absorption, the criteria for determination of the detection wavelengths is stringent. Another issue is the determination of these parameters without going outside the bounds that determine the conditions for the high detectivity.

5.1 MBE Growth of the Epilayer Structure

The epilayer structures consist of alternating layers of $Al_xGa_{1-x}As$ and strained $In_yGa_{1-y}As$ materials. In addition to the need for adjustment of the mole fractions of these

materials to the desired values, the correct substrate temperature for the growth of strained layers with good crystal quality is also a concern in the growth process.
The doping of the GaAs layers was calibrated likewise the doping calibrations made on $In_{0.53}Ga_{0.47}As$ on InP. However, it is not possible to measure the doping in the strained $In_xGa_{1-x}As$ structures without using complex techniques like secondary ion mass spectroscopy (SIMS), since they can be grown to very thin layers before relaxation. Therefore the doping levels of these alloys are adjusted by linear interpolation between the data of GaAs and $In_{0.53}Ga_{0.47}As$.

5.1.1 Optimization of $Al_xGa_{1-x}As$ and $In_yGa_{1-y}As$ Compositions

$Al_xGa_{1-x}As$ compositions of approximately 0.4 were used for the realization of MWIR QWIP layers on GaAs substrates. Since the concentration of Al was not changed along the structure, for one growth only one aluminum flux was calibrated. The compositions of these layers were directly measured from the multi quantum well samples grown using XRD rocking curves. To obtain the values of the composition and thickness of the quantum wells from these measurements, the results of the measurement were fitted with calculations of the software which simulates the measurement according to the thickness and composition values entered by the user.

After the measurements on the initially grown samples, the value of the aluminum flux was changed to obtain the desired Al mole fraction, while leaving the gallium flux constant. Once gallium flux is held constant, the indium flux can be changed during the quantum well regions to adjust the indium mole fraction, which was changed from one color to another.

The mole fraction of indium in the $In_yGa_{1-y}As$ quantum wells was also characterized by X-ray diffraction as done in the $Al_xGa_{1-x}As$. An example of X-ray diffraction rocking

curve for a two color voltage switchable QWIP sample is given in Figure 28. The main peak in the rocking curve results from the GaAs substrate. The small "satellite" peaks are due to the periodic nature of the QWIP structure. The period and intensity of these satellite peaks are determined by the thickness of quantum well period and compositions of $Al_xGa_{1-x}As$ and $In_yGa_{1-y}As$ layers. Since there are two different QWIP stacks, two different satellite peak series can be seen.

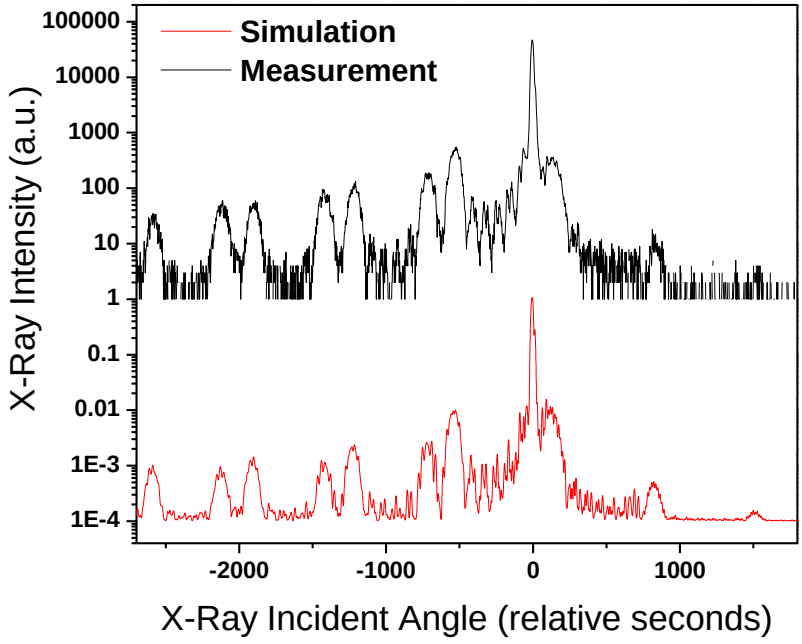

Figure 28: X-ray diffraction rocking curve for a two color voltage switchable QWIP sample and the simulated rocking curve.

5.1.2 Optimization of Substrate Temperature

The adjustment of temperature for $In_xGa_{1-x}As$ layers grown on GaAs substrates was studied to obtain better material quality. The dependence of the $In_xGa_{1-x}As$ critical thickness to the temperature was investigated by Ekenstedt et.al [56] on bulk material. Their experimental results supported by models of growth can be seen in Figure 29. The results show that there is a drastic increase in the critical thickness from 10 Å to 95 Å when the substrate temperature is decreased from 590°C to 490°C for indium mole fraction of 0.36. Our structures has similar indium mole fraction and the deposited $In_xGa_{1-x}As$ layers were around 30Å thick each, leading a total thickness around 200-300 Å depending on the number of periods. When the strained $In_xGa_{1-x}As$ material is grown between thick barrier materials, the relaxation is found to happen at larger critical thickness [57]. However, the critical thickness at usual growth temperatures is below the thickness of one well region. Therefore to minimize the probability of relaxation, together with prevention of indium desorption from the surface which tends to happen above 500 °C [58], the temperature of the substrate during the growth was decreased to 490 °C. This temperature gives a safe margin for growth.

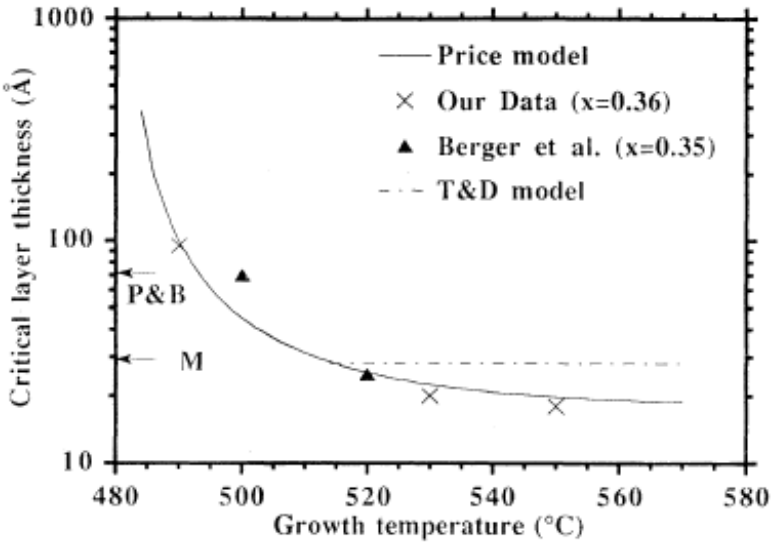

Figure 29: The experimentally obtained and calculated critical layer thicknesses as a function of substrate temperature. [56].

5.2 FPA Performance

The epilayer structure of this sample can be seen in Figure 30. Using this material, a 640×512 FPA was fabricated.

The fabricated FPA utilizes single indium bump per pixel approach. The advantages of this approach were discussed in detail in section 2.3. After the fabrication, the FPA was flip chip bonded to Indigo ISC9803 ROIC and the substrate was removed. ISC9803 ROIC is capable of applying bias voltages to the FPA ranging between zero and -3.5 Volts. The QWIP structure was optimized for switching between two wavelengths when the applied bias is in this range.

For characterization of the FPA, test pixels identical to the FPA pixels were prepared as done for the InP based MWIR QWIP. The responsivity spectrum of the test detectors were measured using the FTIR spectrometer setup described in section 4.2. In this measurement, the FTIR system was purged continuously by N_2 gas . As a result of purging, the concentration of CO_2 inside the system was reduced and the responsivity spectra were obtained more clearly.

The obtained spectra are given in Figure 31. At 1 V reverse bias, color 1 has peak at 4.1 μm with cutoff wavelengths of 3.95 and 4.2 μm. The color 2 peak at this bias is at 4.7 μm having 37% intensity of color 1. Under 3.5 V reverse bias, the peak is at 4.7 μm, having cutoff wavelengths of 4.25 μm and 4.95 μm. At 4.1 μm the responsivity is 40% of color 2 peak.

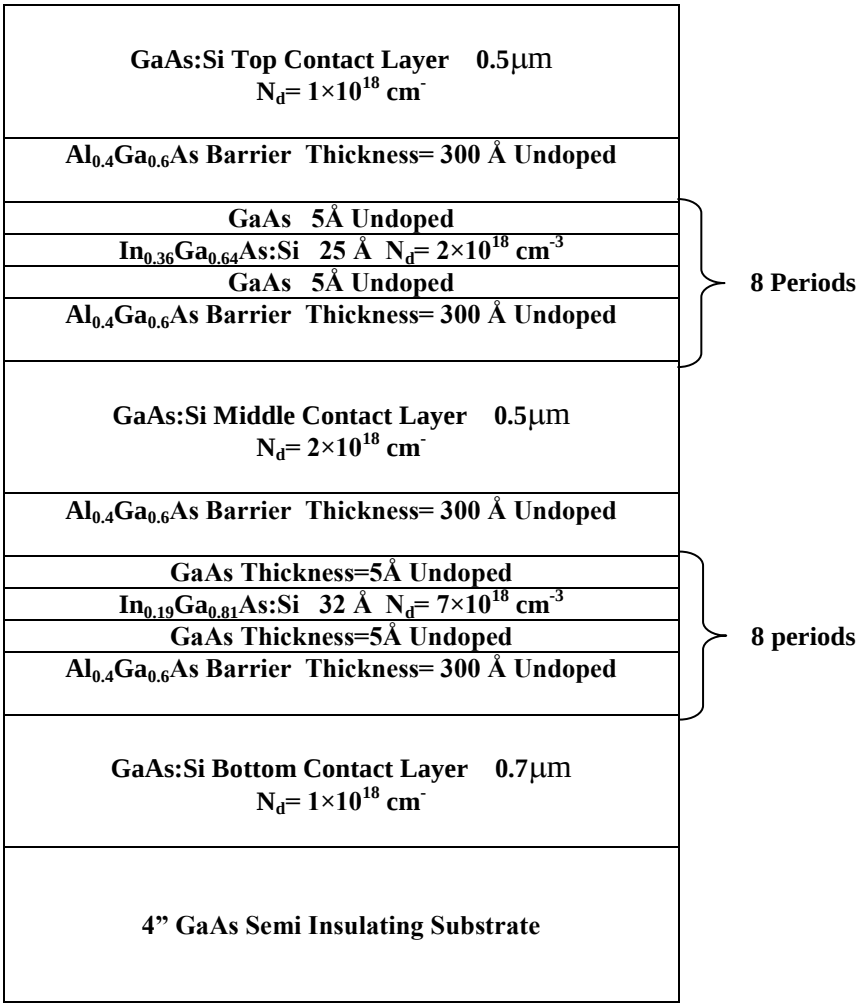

Figure 30: The epilayer structure of the voltage switchable MWIR/MWIR QWIP.

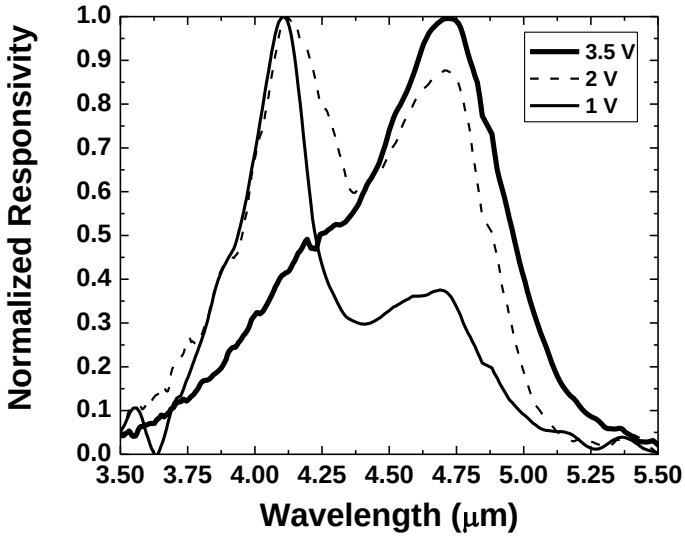

Figure 31: The responsivity spectra measured on test structures identical to FPA pixels. The voltage switching behavior can clearly be seen.

Figure 32 shows the dark current versus bias characteristics of the test pixels at 77 K detector temperature, as well as the photocurrent obtained with f/1.5 aperture and 300 K background temperature. The detector exhibits BLIP characteristic up to a reverse bias voltage of 3.8 V at 77 K operating temperature.

The peak detectivity of the detector was calculated using noise gain, current versus voltage, responsivity and responsivity spectrum data by the help of equation 9. Figure 33 shows the bias dependence of the peak detectivity of the test pixels measured at 77 K detector temperature and f/1.5 aperture. The peak detectivity of ~5.5×10^{10} is obtained for both colors under 300 K background. The detectivity rapidly decreases for bias voltages larger than 3.5 V, possibly due to the onset of impact ionization. The estimated quantum efficiency of the detector is ~1.5 % in color 1 mode and ~5 % in color 2 mode. It should

be noted that this η value directly reflects the absorption characteristic of the FPA pixels due to the identical structures of the test detectors and FPA pixels.

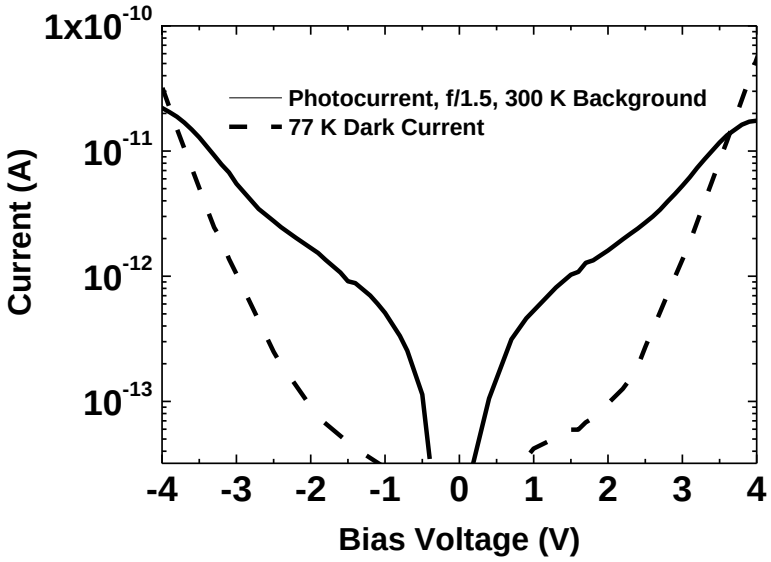

Figure 32: The dark current and photocurrent values obtained for one MWIR/MWIR QWIP FPA pixel.

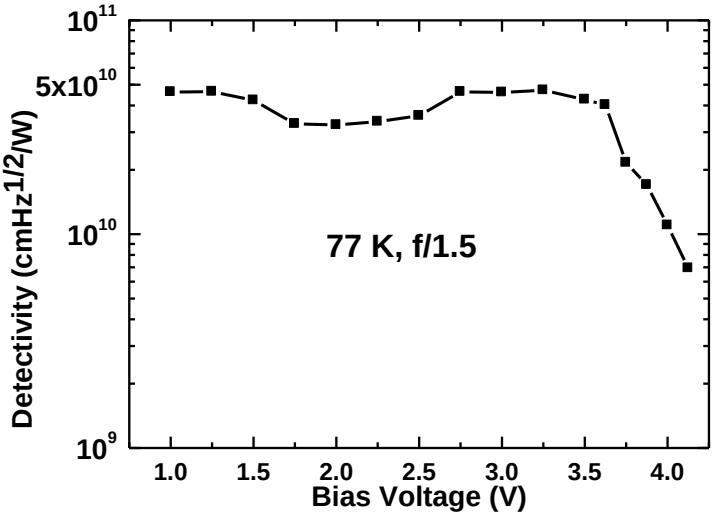

Figure 33: The peak detectivity of the MWIR/MWIR QWIP as a function of reverse bias voltage.

NETD, operability and non uniformity of the detector were measured at 80K with f/1.5 aperture as described in section 4.2. As a rule of thumb, the NETD measurements were done with the ROIC capacitors half-filled. Half–filled ROIC capacitors provide the largest dynamic range in the target radiance. To adjust the capacitors to half-filled situation for a given bias, the integration time was changed. However, since the current passing through one pixel for the detector investigated was not enough to fill the ROIC capacitors to half, even under 3.5V bias with the maximum possible integration time of 20 ms , all of the measurements were done with 20 ms integration time. The FPA was found to provide operability of 99.5% approximately with an uncorrected DC signal non–uniformity of 8.5%.

Although the detectivity of the pixels is very close in both color1 mode and color 2 mode, the NETD values measured on FPA had substantial difference. This situation is the result of the noise coupled from external sources to the test setup. One should bear in mind that the utilized ROIC was optimized mainly for the LWIR arrays, which have current significantly higher than the MWIR arrays. Therefore, the signal obtained is weak and much prone to external noise, especially under low bias conditions used for color1 mode. The NETD values were also calculated from the detectivity values by the help of equation 13. These values are thought to be closer to the real condition. The calculated NETD values are given in Figure 35. The NETD values indicate that the series connection of two MQW stacks has no significant degrading effect on the performance.

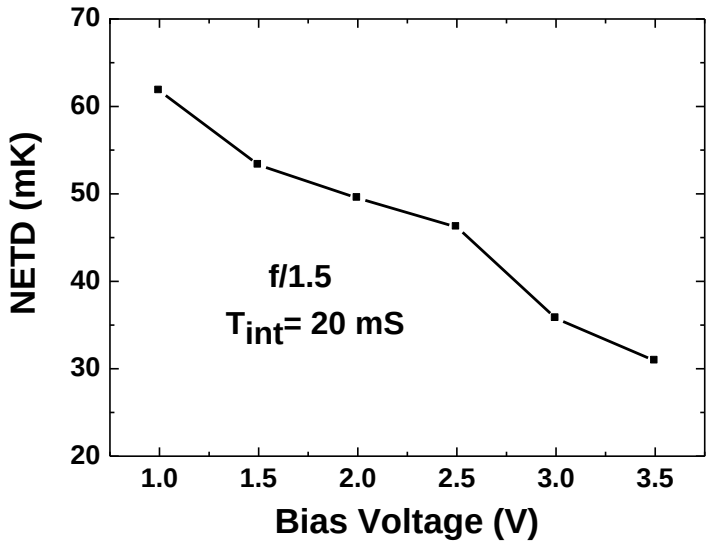

Figure 35: The NETD of the MWIR/MWIR QWIP at 77 K operating temperature with f/1.5 aperture, 20ms integration time and 300 K background temperature.

Although the FPA is intended to use in two colors on frame by frame basis, for trial of the FPA, images were obtained by manually adjusting a single color camera between two bias levels while keeping the scene steady. In Figure 36 the image of a person and a soldering iron at 400°C is seen first in color1 mode then in color 2 mode. The third image was obtained by dividing the color 2 data by color 1 data. Some details like the beard of the person or the crinkles of the cloth are more pronounced in the divided image.

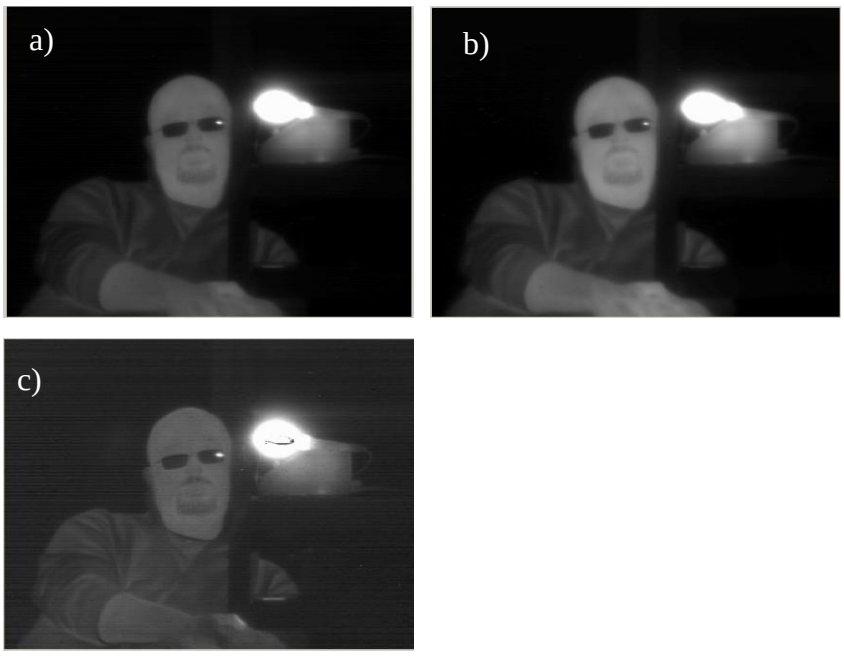

Figure 36: The images of a person and a soldering iron obtained a) in color 1 mode b) in color 2 mode and the image c) obtained by dividing color 2 data by color 1 data.

In Figure 37, the image of a person holding a hot object in his hand is seen. In the image taken with color 1 the hot object, its reflection on the car and the reflection of the Sun on

the car can be distinguished. However, in the second image taken with color 2, the reflection of the Sun is not seen while the reflection of the hot object can be seen.

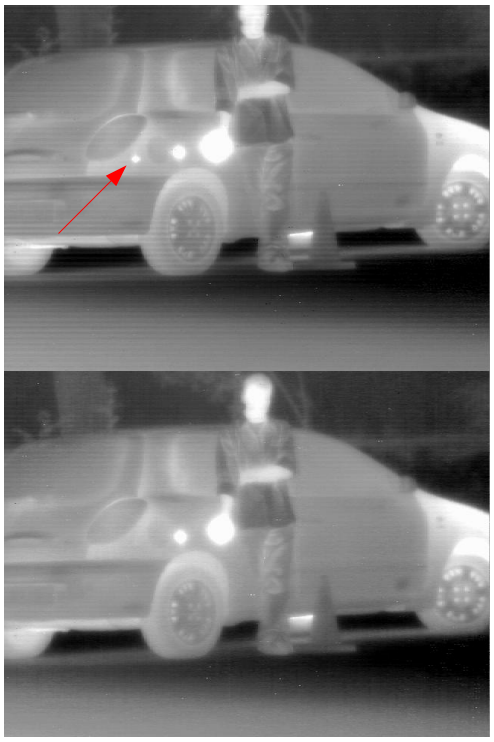

Figure 37: The images of a person and a car obtained with color 1 (up) and color 2 (down) modes respectively. The reflection of the Sun from the car body is marked with the red arrow.

Since the resistance of the multi quantum well stacks decrease with the illumination level on the stack, one might claim that the bias distribution between the stacks can change under illumination with light having different spectral distribution. This kind of change is expected to cause a change in the responsivity spectrum of the detector. To investigate this phenomenon, at the biases -1 V and -3.5 V three sets of spectra were obtained under different illumination conditions, using a blackbody source at 500 °C and 750 °C

together with a SiC heating element having color temperature of 1000 °C. The spectra at -1 V can be seen in Figure 38 while the spectra at -3.5 V are given in Figure 39. It must be mentioned that, the current passing through the detector exposed to radiation from 500°C source (at a distance) was almost same with current of the detector when exposed to 300 K background, while the current was more than two times of this value under exposure of SiC source. As it can be seen from the figures, the deviation in the responsivity spectra under different target temperatures is minimal and within the limits of experimental error. Actually since the wavelength range of two colors is very close to each other, they will be affected from the decrease of resistance at similar amounts resulting in a small net change in the voltage distribution on the two stacks.

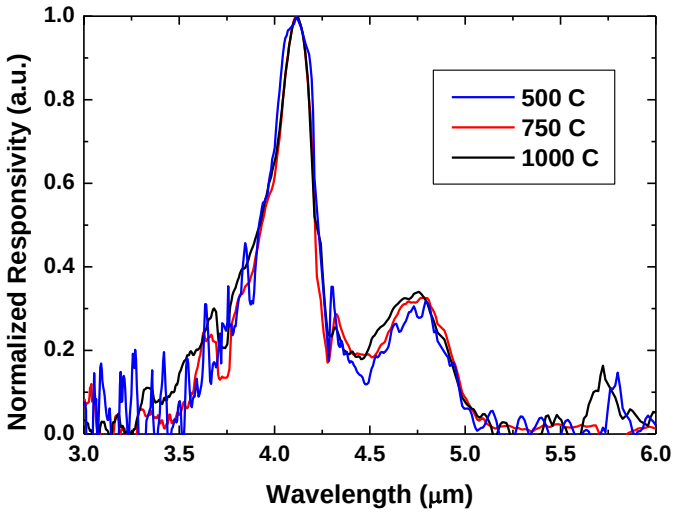

Figure 38: Responsivity spectra of the MWIR/MWIR QWIP at -1 V bias for different target temperatures.

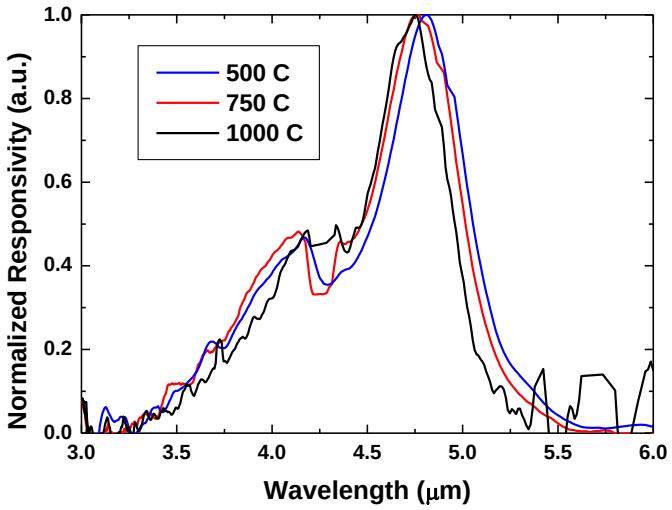

Figure 39: Responsivity spectra of the MWIR/MWIR QWIP at -3.5 V bias for different target temperatures.

5.4 Conclusion

A large format (640x512) voltage tunable dual color MWIR/MWIR QWIP FPA was reported for the first time. The results of this work, displaying the promise of the approach, are quite encouraging for further study towards the optimization of the device structure for achieving low cost, large format dual color MWIR FPA. It should be noted that the ROIC utilized in this work is not optimized for this application and lower electron capacity ROIC alternatives with lower noise levels are commercially available. Furthermore, the FPA performance can considerably be improved by optimizing the optical grating structure.

CHAPTER 6

CONCLUSION AND FURTHER WORK

In this thesis work, MWIR and dual color MWIR/MWIR QWIP FPAs were fabricated and their performance was assessed. The results obtained are promising for the future production of dual color large or very large format high performance FPAs in the MWIR band.

The MWIR QWIP devices have considerably lower dark current compared to the LWIR devices. Also the photon flux in the MWIR band is less compared to LWIR, for objects near room temperature causing less photocurrent. Therefore both the signal and the noise are reduced. Though the detectivity (and thus signal to noise ratio) of the MWIR QWIPs is larger than LWIR counterparts, because of their lower signal levels the MWIR QWIPs are affected more from the noise of the ROIC and the noise coupled from environment. Since the ROIC which was available during this work was optimized for LWIR detection, the ROIC integration capacitance value was large. This large capacitance value created larger noise. Because of the effects of this large ROIC noise and external noise, the real performance of the MWIR QWIPs may be underestimated. In the later stages of development of the MWIR QWIP FPAs, using ROICs optimized for the needs of these detectors will improve the performance surely. Even though there was a handicap caused by ROICs, the studied sensor exhibited performance close to the state of the art devices.

InP based MWIR QWIP devices has the advantage to be combined with the LWIR devices to form dual band arrays. However, fabricating dual color MWIR/MWIR detectors by using lattice matched $In_{0.52}Al_{0.48}As/In_{0.53}Ga_{0.47}As$ material system does not seem to be possible, since the spectrum broadens too much when the quantum well thickness is adjusted so that detection at wavelengths close to 5 μm is observed. The broadening of the spectrum will cause high spectral cross talk between two colors. To increase the detection wavelength, while keeping a narrow responsivity spectrum, different alloys such as InGaAlAs or InGaAsP may be used as the quantum well material. Since the bandgap of these alloys can be tuned to higher values than $In_{0.53}Ga_{0.47}As$, the conduction band discontinuity between the well and the barrier will decrease, resulting in an increase in the detection wavelength. Furthermore these two quaternary alloys are also lattice matched to the InP substrates in a wide range of compositions, the advantages of the lattice matched growth would not be degraded.

Also doping of the structure may be increased if the FPAs will be cooled to 77 K during operation. Dark current will increase as a result of the increase in doping, however at temperatures around 77 K dark current will still be negligible. Thus FPA performance may increase with increasing responsivity.

The MWIR/MWIR QWIP can be improved by the used of better optimized diffraction grating. There may also be some tuning on the detection wavelengths of the colors depending on the application and perhaps the infrared signatures of targets. This design can be scaled to arrays having very large format, adding megapixel multi spectral imaging capability to the QWIPs.

REFERENCES

[1] Cellek, O.O., Ozer, S., Besikci, C., "High responsivity InP-InGaAs quantum-well infrared photodetectors: Characteristics and focal plane array performance", IEEE Journal of Quantum Electronics, vol.41, pp. 980-985, 2005

[2] Ozer, S., Tumkaya, U., Asici, B., Besikci, C., "Demonstration and performance assessment of large format InP-InGaAsP quantum-well infrared photodetector focal plane array", IEEE Journal of Quantum Electronics, vol. 43, pp. 709-713, 2007

[3] Schneider, H., Liu, H.C., "Quantum Well Infrared Photodetectors", Springer-Verlag Berlin Heidelberg, 2007

[4] Wikimedia Foundation, "Black –body spectrum",*http://upload.wikimedia.org /wikipedia/commons/thumb/f/ff/BlackbodySpectrum_loglog_150dpi_en.png/800px-BlackbodySpectrum_loglog_150dpi_en.png* , 20.08.2008

[5] Wikimedia Foundation, "Infrared", *http://en.wikipedia.org/wiki/Infrared*, 20.08.2008

[6] Fraenkel, A., Mizrahi, U., Bykov, L., Adin, A., Malkinson, E., Zabar, Y., Seter, D., Gebil, Y., Kopolovich, Z., "Advanced features of SCD's uncooled detectors", Opto-electronics Review, vol. 14, pp. 47-54, 2006.

[7] Schneider, H., Walther, M., Schonbein, C., Rehm, R., Fleissner, J., Pletschen, W.,Braunstein, J., Koidl, P., Weimann, G., Ziegler, J., Cabanski, W. , "QWIP FPAs for high-performance thermal imaging", Physica E, vol. 7, pp 101-107, 2000

[8] King, D.F., Radford, W.A., Patten, E.A., Graham, R.W., McEwan, T.F., Vodicka, J.G., Bornfreund, R.E., Goetz, P.M., Venzor, G.M., Johnson, S.M., Jensen, J.E., Nosho, B.Z., Roth, J.A., "3rd-generation 1280 × 720 FPA development status at Raytheon Vision Systems", Proceedings of SPIE, vol. 6206, 62060W-1, 2006

[9] Cabanski, W., Mu̇nzberg, M., Rode, W., Wendler, J., Ziegler, J., Fleißner, J., Fuchs, F., Rehm, R., Schmitz, J., Schneider, H., Walther, M. , "Third generation focal plane array IR detection modules and applications" Proceedings of SPIE, vol. 5783, pp. 340-349, 2005

[10] Costard, E., Bois, Ph., "THALES long wave QWIP thermal imagers", Infrared Physics and Technology, vol.50, pp. 260-269, 2007

[11] Rehm, R., Schneider, H., Walther, M., Koidl, P., Weimann, G., "Avalanche multiplication due to impact ionization in quantum-well infrared photodetectors: A quantitative approach", Applied Physics Letters ,vol. 82 , pp. 2907-2909 , 2003

[12] Schneider, H., "Theory of avalanche multiplication and excess noise in quantum-well infrared photodetectors", Applied Physics Letters, vol. 82, pp. 4376-4378, 2003

[13] Nötzel, R., "Self-organized growth of quantum-dotstructures", Semicond. Science. And Technology, vol. 11, pp.1365–1379, 1996

[14] Gunapala, S.D., Bandara, S.V., Hill, C.J., Ting, D.Z., Liu, J.K., Rafol, S.B., Blazejewski, E.R., Mumolo, J.M., Keo, S.A., Krishna, S., Chang, Y.-C., Shott, C.A., "640 × 512 pixels long-wavelength infrared (LWIR) Quantum-Dot Infrared Photodetector (QDIP) imaging focal plane array", IEEE Journal of Quantum Electronics, vol. 43, pp. 230-237, 2007

[15] Liu, H.C., Gao, M., McCaffrey, J., Wasilewski, Z.R., Fafard, S., "Quantum dot infrared photodetectors" , Applied Physics Letters , vol.78 , pp. 79-81 , 2001

[16] Krishna , S., “Quantum dots-in-a-well infrared photodetectors”, Infrared Physics and Technology, vol. 47, pp. 153-163, 2005

[17] Levine, B.F. , “Quantum Well Infrared Photodetectors”, Journal of Applied Physics vol.74 (8), pp. R1-R81, 1993

[18] Bois, P., Costard, E., Marcadet, X., Herniou, E. , “Development of quantum well infrared photodetectors in France”, Infrared Physics and Technology , vol.42, pp. 291-300 , 2001

[19] Choi, K.-K., Monroy, C., Swaminathan, V., Tamir, T., Leung, M., Devitt, J., Forrai, D., Endres, D., “Optimization of corrugated-QWIPs for large format, high quantum efficiency, and multi-color FPAs”, Infrared Physics and Technology , vol. 50 , pp. 124-135 , 2007

[20] Choi, K.K., Lin, C.H., Leung, K.M., Tamir, T., Mao, J., Tsui, D.C., Jhabvala, M., “Broadband and narrow band light coupling for QWIPs”, Infrared Physics and Technology, vol. 44, pp. 309-324, 2003

[21] Liu, H.C., “Photoconductive gain mechanism of quantum-well intersubband infrared detectors”, Applied Physics Letters, vol. 60, pp. 1507-1509, 1992

[22] Steele, A.G., Liu, H.C., Buchanan, M., Wasilewski, Z.R., “Influence of the number of wells in the performance of multiple quantum well intersubband infrared detectors”, Journal of Applied Physics, vol. 72, pp. 1062-1064, 1992

[23] Urayama, J., Norris, T.B., Singh, J., Bhattacharya, P., “Observation of phonon bottleneck in quantum dot electronic relaxation”, Physical Review Letters , vol. 86, pp. 4930-4933, 2001

[24] Choi, K.K., Bandara, S.V., Gunapala, S.D., Liu, W.K., Fastenau, J.M. , “Detection wavelength of InGaAs/AlGaAs quantum wells and superlattices” , Journal of Applied Physics , vol. 91 , pp. 551-564, 2002

[25] Razeghi, M., Erdtmann, M., Jelen, C., Guastavinos, F., Brown, G.J., Park, Y.S. , "Development of quantum well infrared photodetectors at the Center for Quantum Devices" , Infrared Physics and Technology , vol. 42, pp. 135-148 , 2001

[26] Cellek, O.O., Besikci, C., "Detailed investigation of electron transport, capture and gain in Al 0.3Ga 0.7As/GaAs quantum well infrared photodetectors", Semiconductor Science and Technology , vol. 19 , pp. 183-190 , 2004

[27] Zhang, W., Lim, H., Taguchi, M., Tsao, S., Movaghar, B., Razeghi, M., "High-detectivity InAs quantum-dot infrared photodetectors grown on InP by metal-organic chemical-vapor deposition" , Applied Physics Letters , vol. 86 , pp. 1-3 , 2005

[28] Tsao, S., Lim, H., Seo, H., Zhang, W., Razeghi, M., "InP-based quantum-dot infrared photodetectors with high quantum efficiency and high-temperature imaging ", IEEE Sensors Journal , vol. 8 , pp. 936-941, 2008

[29] Pires, M.P., Landi, S.M., Tribuzy, C.V.-B., Nunes, L.A., Marega, E., Souza, P.L., "InAs quantum dots over InGaAs for infrared photodetectors" , Journal of Crystal Growth vol. 272 , pp. 192-197 , 2004

[30] Gunapala, S.D., Bandara, S.V., Liu, J.K., Mumolo, J.M., Hill, C.J., Rafol, S.B., Salazar, D.cWoolaway, J., LeVan, P.D., Tidrow, M.Z., "Towards dualband megapixel QWIP focal plane arrays" , Infrared Physics and Technology , vol. 50, pp. 217-226 , 2007

[31] Sundaram, M., Wang, S.C., Taylor, M.F., Reisinger, A., Milne, G.L., Reiff, K.B., Rose, R.E., Martin, R.R., "Two-color quantum well infrared photodetector focal plane arrays" , Infrared Physics and Technology vol. 42 , pp. 301-308 , 2001

[32] Schneider, H., Maier, T., Fleissner, J., Walther, M., Koidl, P., Weimann, G., Cabanski, W., Finck, M., Menger, P., Rode, W., Ziegler, J., "High-resolution 3-

5μm/8-12 μ dual-band quantum well infrared photodetector array" , Electronics Letters , vol. 40 , pp. 831-833, 2004

[33] Varley, E., Lenz, M., Lee, S.J., Brown, J.S., Ramirez, D.A., Stintz, A., Krishna, S., Reisinger , A., Sundaram, M., "Single bump, two-color quantum dot camera", Applied Physics Letters , vol. 91 , art. no. 081120 , 2007

[34] Gray, A.L., Stintz, A., Malloy, K.J., Newell, T.C., Lester, L.F., "Morphology and relaxation in InyGa1-yAs/GaAs multi-layer structures" , Journal of Crystal Growth , vol. 222 , pp. 726-734 , 2001

[35] Chui, H.C., Martinet, E.L., Fejer, M.M., Harris Jr., J.S., "Short wavelength intersubband transitions in InGaAs/AlGaAs quantum wells grown on GaAs " , Applied Physics Letters , vol. 64 , pp. 736-738 ,1994

[36] Levine, B.F.,Cho, A.Y.,Walker, J.,Malik, R.J.,Kleinman, D.A.,Sivco, D.L., "InGaAs/InAlAs multiquantum well intersubband absorption at a wavelength of λ=4.4 μm" , Applied Physics Letters,vol. 52,pp. 1481-1483 , 1988

[37] Hasnain, G.,Levine, B.F.,Sivco, D.L.,Cho, A.Y., "Mid-infrared detectors in the 3-5 μm band using bound to continuum state absorption in InGaAs/InAlAs multiquantum well structures" , Applied Physics Letters, vol. 56, pp. 770-772., 1990

[38] Ozer, S., Tumkaya, U., Besikci, C., "Large format AlInAs-InGaAs quantum-well infrared photodetector focal plane array for midwavelength infrared thermal imaging" , IEEE Photonics Technology Letters , vol. 19 , pp. 1371-1373, 2007

[39] Shanabrook, B.V., Waterman, J.R., Davis, J.L., Wagner, R.J., "Large temperature changes induced by molecular beam epitaxial growth on radiatively heated substrates" , Applied Physics Letters , vol. 61 , pp. 2338-2340 , 1992

[40] Johnson, S.R., Grassi, E., Beaudoin, M., Boonzaayer, M.D., Tsakalis, K.S., Zhang, Y.-H. , "Feedback control of substrate temperature during the growth of

near-lattice-matched InGaAs on InP using diffuse reflection spectroscopy", Journal of Crystal Growth, vol. 201, pp. 40-44, 1999

[41] Roth, J.A., Chow, D.H., Olson, G.L., Brewer, P.D., Williamson, W.S., Johs, B., "Real-time control of the MBE growth of InGaAs on InP" , Journal of Crystal Growth , vol. 201, pp. 31–35, 1999

[42] McElhinney, M., Stanley, C.R., "Reduced indium incorporation during the MBE growth of In(Al,Ga)As" , Electronics Letters , vol. 29, pp. 1302–1304, 1993

[43] Schneider, H., Maier, T., Fleissner, J., Walther, M., Koidl, P., Weimann, G., Cabanski, W., Finck, M., Menger, P., Rode, W., Ziegler, J., "Dual-band QWIP focal plane array for the second and third atmospheric windows" , Infrared Physics and Technology vol. 47, pp. 53–58, 2005

[44] De Rossi, A., Costard, E., Guerineau, N., Rommeluere, S., "Effect of finite pixel size on optical coupling in QWIPs" , Infrared Physics and Technology , vol. 44 , pp. 325-330 , 2003

[45] Donchev, V., Bourgoin, J.C., Bois, P., "Dark current through GaAs/AlGaAs multiple quantum wells" , Semiconductor Science and Technology , vol. 17 pp. 621-624 , 2002

[46] Brennan , K. F., Brown , A.S., "Theory Of Modern Electronic Semiconductor Devices" , John Wiley &Sons , New York , 2002

[47] Molina, M., Breniere, X., Tribolet, P., "IR detector dewar and assemblies for stringent environmental conditions" , Proceedings of SPIE ,vol. 6542, art. no. 65422N , 2007

[48] Sarusi, G., "QWIP or other alternative for third generation infrared systems" Infrared Physics and Technology ,vol. 44 , pp. 439-444 , 2003

[49] Sanderson, R. B. , “Infrared missile warning sensors” IEEE Proceedings of the National Aerospace and Electronics Conference , vol.2, pp. 777-781 , 1996

[50] Rehm, R., Walther, M., Schmitz, J., Fleißner, J., Ziegler, J., Cabanski, W., Breiter, R. , “Dual-colour thermal imaging with InAs/GaSb superlattices in mid-wavelength infrared spectral range” , Electronics Letters , vol. 42, pp. 577-578, 2006

[51] Tribolet, P., Vnillermet, M., Destefanis, G., “The third generation cooled IR detector approach in France” , Proceedings of SPIE , vol.5964, art. no. 596407 , 2005

[52] Jiang, X., Li, S.S., Tidrow, M.Z. , “Investigation of a multistack voltage-tunable four-color quantum-well infrared photodetector for mid- and long-wavelength infrared detection” , IEEE Journal of Quantum Electronics , vol. 35 , pp. 1685-1692 , 1999

[53] Guzmán, A., Sánchez-Rojas, J.L., Tijero, J.M.G., Hernando, J., Calleja, E., Muñoz, E., Vergara, G., Almazán, R., Sánchez, F.J., Verdú, M., Montojo, M.T., “Voltage-tunable two-colour quantum well infrared detector with Al-graded triangular confinement barriers” Semiconductor Science and Technology , vol. 16, pp. 285-288 , 2001

[54] Rauter, P., Fromherz, T., Bauer, G., Diehl, L., Dehlinger, G., Sigg, H., Grϋtzmacher, D., Schneider, H., “Voltage-tunable, two-band mid-infrared detection based on Si/SiGe quantum-cascade injector structures” , Applied Physics Letters ,vol. 83, pp. 3879-3881, 2003

[55] Lenchyshyn, L.C., Liu, H.C., Buchanan, M., Wasilewski, Z.R. , “Voltage-tuning in multi-color quantum well infrared photodetector stacks” , Journal of Applied Physics vol. 79 , pp. 8091-8097 , 1996

[56] Ekenstedt, M.J., Andersson, T.G., Wang, S.M., “Temperature-dependent relaxation and growth phenomena in strained InxGa1-xAs layers grown on GaAs” , Physical Review B , vol. 48 , pp. 5289-5299 , 1993

[57] Gourley, P.L., Fritz, I.J., Dawson, L.R. , “Controversy of critical layer thickness for InGaAs/GaAs strained-layer epitaxy” , Applied Physics Letters , vol. 52 , pp. 377-379, 1988

[58] Jackson, A., Pinsukanjana, P., Coldren, L., Gossard, A., “Monitoring Ga and In desorption and In surface segregation during MBE using atomic absorption”, Journal of Crystal Growth , vol. 175-176 (PART 1), pp. 244-249 , 1997